Space Systems

STAR SENSOR/MAPPER WITH A SELF-DEPLOYABLE, HIGH-ATTENUATION LIGHT SHADE FOR SAS-B

by F. W. SCHENKEL AND A. FINKEL

THE JOHNS HOPKINS UNIVERSITY ▪ APPLIED PHYSICS LABORATORY

APL/JHU

CP 017

JULY 1972

Space Systems

STAR SENSOR/MAPPER WITH A SELF-DEPLOYABLE, HIGH-ATTENUATION LIGHT SHADE FOR SAS-B

by F W. SCHENKEL AND A FINKEL

THE JOHNS HOPKINS UNIVERSITY ● APPLIED PHYSICS LABORATORY
8621 Georgia Avenue ○ Silver Spring, Maryland   20910

Page intentionally left blank

ABSTRACT

The Small Astronomy Satellites (SAS) require a star sensor/mapper to yield satellite positional data for the purpose of determining the orientation of a specific stellar experimental payload. The orbit is equatorial at an altitude of 550 km, with an arbitrary satellite spin-axis orientation. In the case of the SAS-B satellite, spin rates of 1/12 and 1 rpm must be accommodated.

The star sensor/mapper has been tested to detect stars of +4 visual magnitude. It utilizes two information channels with memory so that it can be used with a low-data-rate telemetry system. One channel yields star amplitude information, the other yields the time of star occurrence as the star passes across an "N" slit reticle/photomultiplier detector system. Some of the unique features of the star sensor/mapper are its low weight of 6.5 pounds, low power consumption of 0.4 watt, bandwidth switching to match the satellite spin rate, optical equalization of sensitivity over the 5° by 10° field of view, and self-deployable sunshade. The attitude determination accuracy is 3 arc minutes. This is determined by such parameters as the reticle configuration, optical train, and telemetry readout.

The optical and electronic design of the star sensor/mapper, its expansion capabilities, and its unique features will be discussed.

ACKNOWLEDGMENT

CONTENTS

Appendixes (Cont'd)

ILLUSTRATIONS

1. SUMMARY

A requirement for the Small Astronomy Satellite-B (SAS-B) was a star sensor to provide satellite positional data to an accuracy of 3 arc minutes for satellite spin rates of 1/12 and 1 rpm. The star sensor is required to detect stars having a +4 visual magnitude during the sunlit portion of the orbit. The spacecraft orientation can be anything achievable in its near-equatorial, 550-km orbit.

The design of the star sensor resulted in an instrument that weighs 6.5 pounds, consumes 0.4 watt, and operates at spin rates ranging from 1/12 to 3 rpm. The instrument design incorporates optical features that provide excellent uniformity of response across the 5° by 10° field of view. The basic design is intended as a building block to be utilized throughout the SAS series of spacecraft. Figure 1 is a photograph of the star sensor/mapper package.
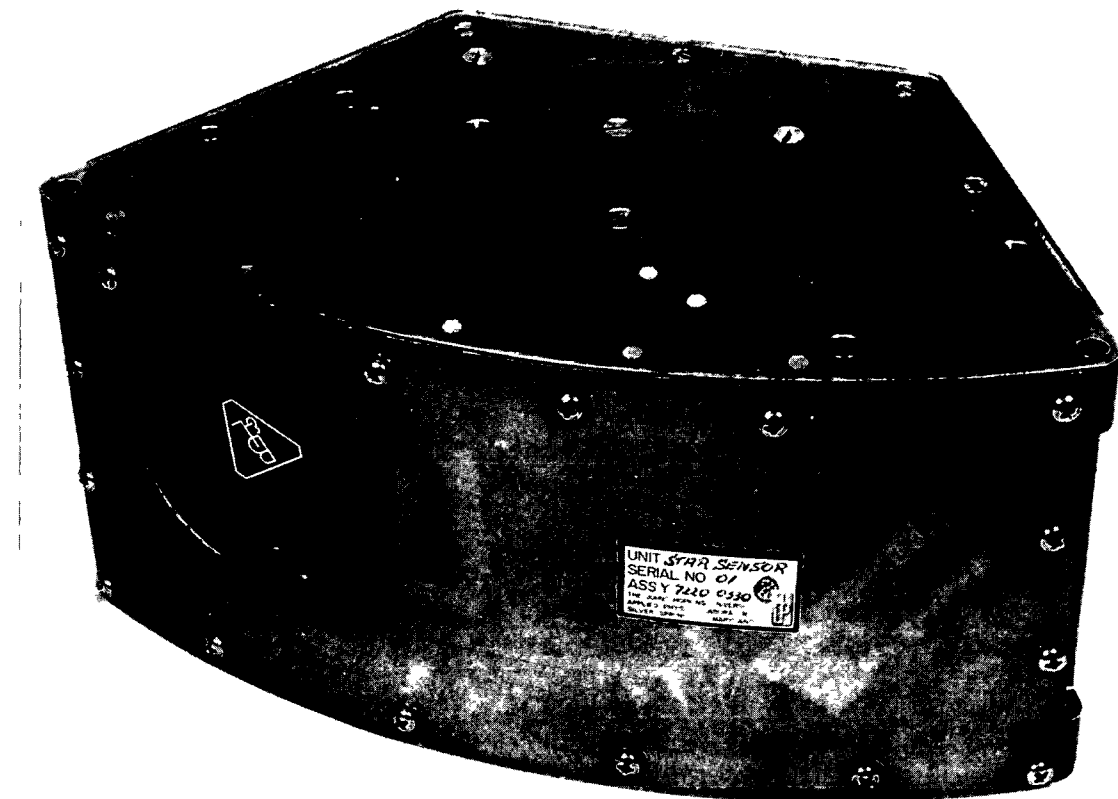
Fig 1   STAR SENSOR PACKAGE

2. GENERAL

The SAS-B spacecraft will be in a circular equatorial orbit at an approximate altitude of 550 km. The spacecraft is spin stabilized, with the direction of the spin vector being arbitrary. The spin rate is to be 1/12 rpm, with a 1-rpm fallback mode. Figure 2 illustrates the relationship of the star mapper to the satellite in its working environment. A continuous measurement of the spacecraft attitude is desired. The signals derived from the star mapper will be stored on tape and read out periodically for ground station data analysis and attitude computation. Based on the spacecraft's requirements, the star sensor is designed to detect stars of +4 visual magnitude with an angular resolution of 3 arc minutes, and to provide sufficient information to permit pitch, roll, and yaw computations. The star mapper will have a field of view of 5° by 10°. The spinning of the spacecraft will result in the sweeping out of a swath 10° wide by 360° every revolution.

The star mapper will have adequate sensitivity to detect stars of +4 visual magnitude (m_v). The sensor will produce time-dependent voltage output pulses to permit star identification on the basis of magnitude and relative position with respect to the satellite coordinate axis.

Figure 3 shows the schematic arrangement of the star mapper constituent components. As the satellite sweeps through a 10° wide swath in the celestial sphere by virtue of its spin, individual stars are imaged on and swept across the "N" shaped slit and detected by a photomultiplier. For a given star, three signal pulses of equal amplitude will result at the photomultiplier tube output. The amplitude of the output signal will be indicative of the star's visual magnitude. The time sequence of the signal pulses will be indicative of the star's location in the star mapper field of view (FOV). By recording the signal magnitudes and relative positions in the star field included in the viewed swath

ARBITRARY ORIENTATION
OF SPIN AXIS

SATELLITE
SAS-B

EQUATORIAL PLANE

EARTH

5°

10°

INDICATES SWATH OF
CELESTIAL SPHERE
COVERED BY STAR
SENSOR

STAR SENSOR
FIELD OF VIEW
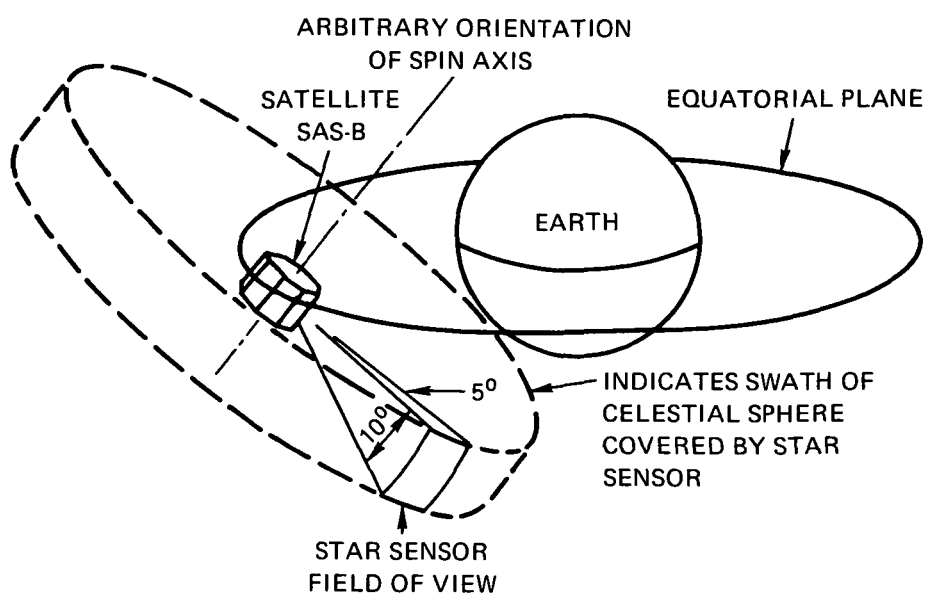
Fig 2   DIAGRAM OF SATELLITE-EARTH ORIENTATION

- 4 -

4" B & L

SUPER BALTAR

FOLDING
MIRROR

"N" RETICLE PLATE

CONDENSER OPTICS

PMT
SENSOR
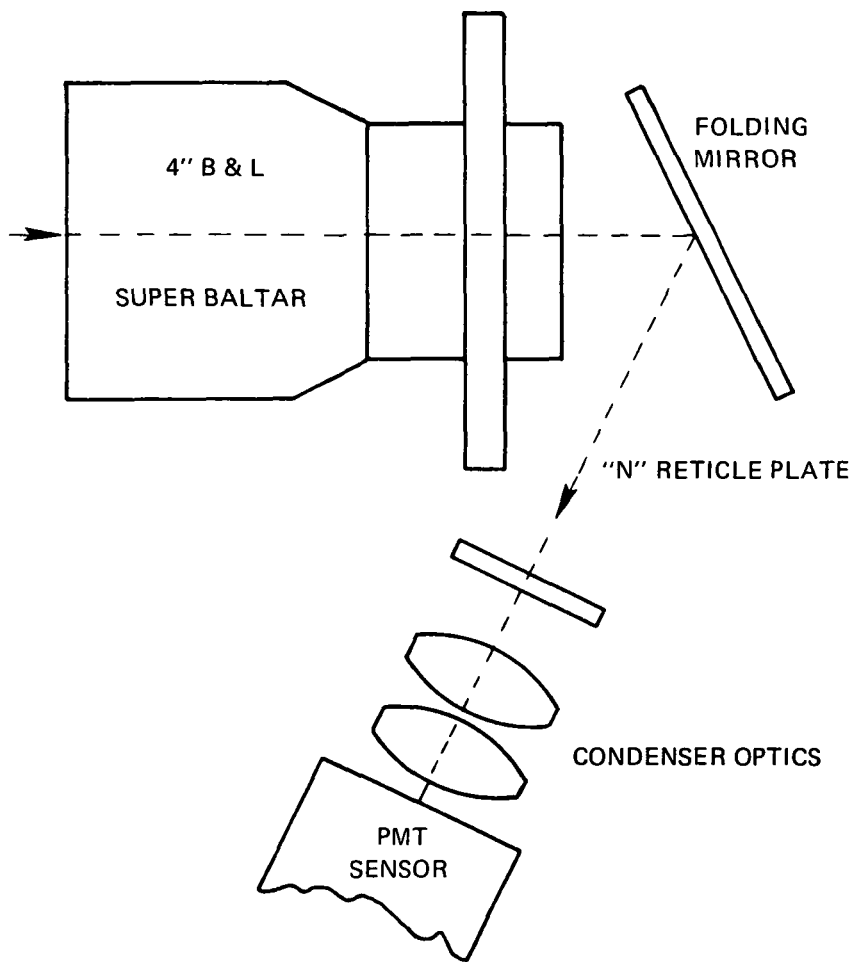
Fig 3   SCHEMATIC OF STAR MAPPER CONSTITUENT COMPONENTS

of the celestial sphere, the satellite attitude is determined. The pulse amplitude and time sequence produced by each star traversing the "N" shaped slit are recorded in the spacecraft simultaneously with a precise clock signal. Appendix A gives a detailed analysis of the star-reticle trajectory computations.

The objective optic used is a Bausch & Lomb Super Baltar, 4-inch focal length, $f/2$ lens. The star image is focused in the plane of the "N" slit reticle. The light rays passing through the slit reticle are collected by a condenser optic and imaged on a fixed 0.25-inch-diameter circular area on the photomultiplier detector. This condenser consists of a pair of double convex lenses 29 mm in diameter. The condenser optic is a significant feature because it makes the amplitude response to a star independent of the star's location in the field of view. The condenser overcomes the problem of photocathode nonuniformity by ensuring that the same area of the sensor photosurface is used at all times, independent of the location of the star image on the "N" slit. The sensor is an EMR type 541E-01-14 with its integrated high-voltage power supply

STAR SPECTRAL PROPERTIES AND PHOTOMETRY

Spectral Properties

Since the star sensor's spectral response does not match that of the eye, stars of equal visual magnitude will not, in general, give equal outputs. Ultimately, NASA will compile a star catalog that will tabulate the sensor's response to each star; therefore a star's visual magnitude is really of no concern. However, it is necessary to relate the response of the sensor to different spectral classes of a given visual magnitude for the following reasons

1. Stars are normally tabulated according to visual magnitude, and it is convenient to be able to speak the same language.

2.   An objective of the star sensor is the ability to detect fourth magnitude stars. It is necessary to ascertain that this ability is indeed achieved for the lower-temperature stars.

3.   Laboratory calibration is performed with a 2870°K light source, which is significantly different from the effective temperature of the stars. It is essential to relate the composite star mapper spectral characteristics to some measurable laboratory photometric quantities. Spectral correction must be applied to retain the meaningfulness of the star sensor transfer characteristic. Mathematically, this compensation can be represented by the factor X

$$X = \frac{\int_0^\infty W_2(\lambda)\, R_s(\lambda)\, d\lambda}{\int_0^\infty W_1(\lambda)\, R_s(\lambda)\, d\lambda} \cdot \frac{\int_0^\infty W_1(\lambda)\, R_e(\lambda)\, d\lambda}{\int_0^\infty W_2(\lambda)\, R_e(\lambda)\, d\lambda} \tag{1}$$

(which equals the relative response of the star sensor to spectral characteristic W_2 compared with its response to characteristic W_1),

where

$W_1(\lambda)$ = power spectral density of source 1 (watts/unit wavelength),

$W_2(\lambda)$ = power spectral density of source 2,

$R_s(\lambda)$ = spectral response of star sensor (amperes/watt), and

$R_e(\lambda)$ = relative sensitivity of eye at wavelength, λ.

Since visual magnitude is defined in terms of the eye's response, the visual magnitudes of two sources, W_2 and W_1, will be in the ratio

- 7 -

$$A = \frac{\int_0^\infty W_2(\lambda) \, R_e(\lambda) \, d\lambda}{\int_0^\infty W_1(\lambda) \, R_e(\lambda) \, d\lambda} \quad . \tag{2}$$

The relative response of the star sensor to these two sources will be the ratio·

$$B = \frac{\int_0^\infty W_2(\lambda) \, R_s(\lambda) \, d\lambda}{\int_0^\infty W_1(\lambda) \, R_s(\lambda) \, d\lambda} \quad . \tag{3}$$

To obtain the relative response of the star sensor to two sources of equal visual magnitude but with spectral characteristics W_2 and W_1, the ratio of Eq. (3) must be normalized by dividing by the ratio of Eq (2), thereby obtaining Eq. (1). Hence, the calculation requires the plotting of the four curves, $W_1(\lambda)$, $W_2(\lambda)$, $R_s(\lambda)$, and $R_e(\lambda)$. The four products, $W_1(\lambda) \, R_s(\lambda)$, $W_1(\lambda) \, R_e(\lambda)$, $W_2(\lambda) \, R_s(\lambda)$, and $W_2(\lambda) \, R_e(\lambda)$, are then obtained and plotted. Finally the four integrals are evaluated by measuring the area under the curves to determine the relative response given by Eq. (1). Note that any arbitrary scale factors associated with W_1, W_2, R_s, or R_e are canceled in the computation so that any convenient scale may be used for each of these quantities. Hence the plotted curves are not normalized, and no attempt should be made to relate one to another except to compare shape.

The relative power spectral density, $W_1(\lambda)$, of a 2870°K black body is shown in Fig. 4. It may be calculated from Planck's law:

$$J(\lambda) \propto \frac{1}{\lambda^5 \, e^{c/\lambda T} - 1} \quad , \tag{4}$$

- 8 -
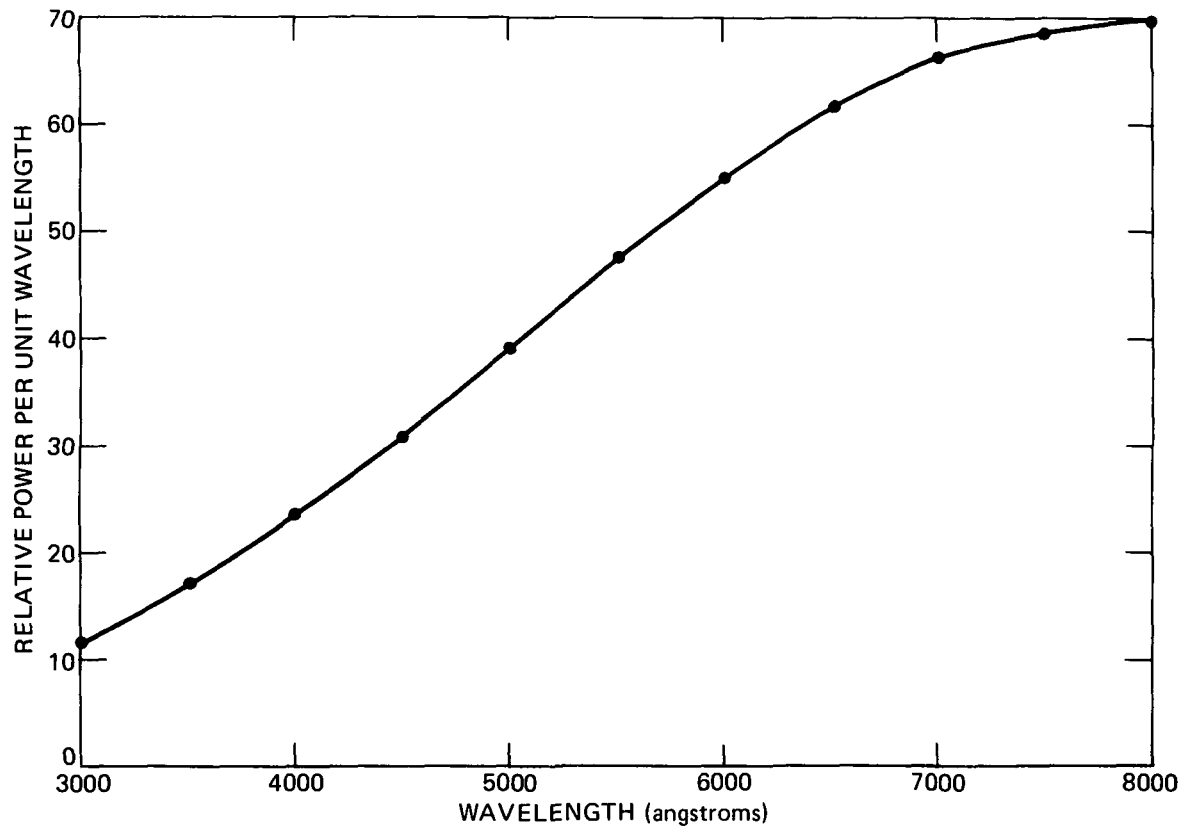
Fig 4 SPECTRAL CHARACTERISTIC OF 2870 °K BLACK-BODY SOURCE

where

λ = wavelength in centimeters, and

c = 1.436 cm-deg.

The S-20 photomultiplier characteristic and the response of the objective lens are shown in Fig. 5. The product of these two curves is the star sensor's spectral characteristic, $R_s(\lambda)$, shown in Fig. 6. Not included in this curve is the effect of the condensing lens in the optical train. This effect, however, is not very significant since primarily this lens will cause further attenuation in the blue region, which is already considerably attenuated by the objective lens.

The standard eye response, $R_e(\lambda)$, is also shown in Fig. 6. The products, $W_1(\lambda) R_e(\lambda)$ and $W_1(\lambda) R_s(\lambda)$, are shown in Fig. 7.

Response to K0 Star. The power spectral density for each star classification may be obtained from Star Trackers and Systems Design by Quasius and McCanless. The characteristic used here is that of a black-body radiator which best approximates that of the star over the full spectrum. The K0 star is given an effective temperature of 4900°K. Using the K0 curves, $W_2(\lambda)$, of this reference, the products with R_e and R_s are formed (Fig. 8).

The areas under the four curves, W_1R_s, W_2R_s, W_1R_e, and W_2R_e, are obtained by counting squares with the aid of Simpson's rule, which results in the following relative areas·

$\int W_1(\lambda) R_e(\lambda) = 770,$

$\int W_1(\lambda) R_s(\lambda) = 874,$

$\int W_2(\lambda) R_e(\lambda) = 776,$

$\int W_2(\lambda) R_s(\lambda) = 841.$
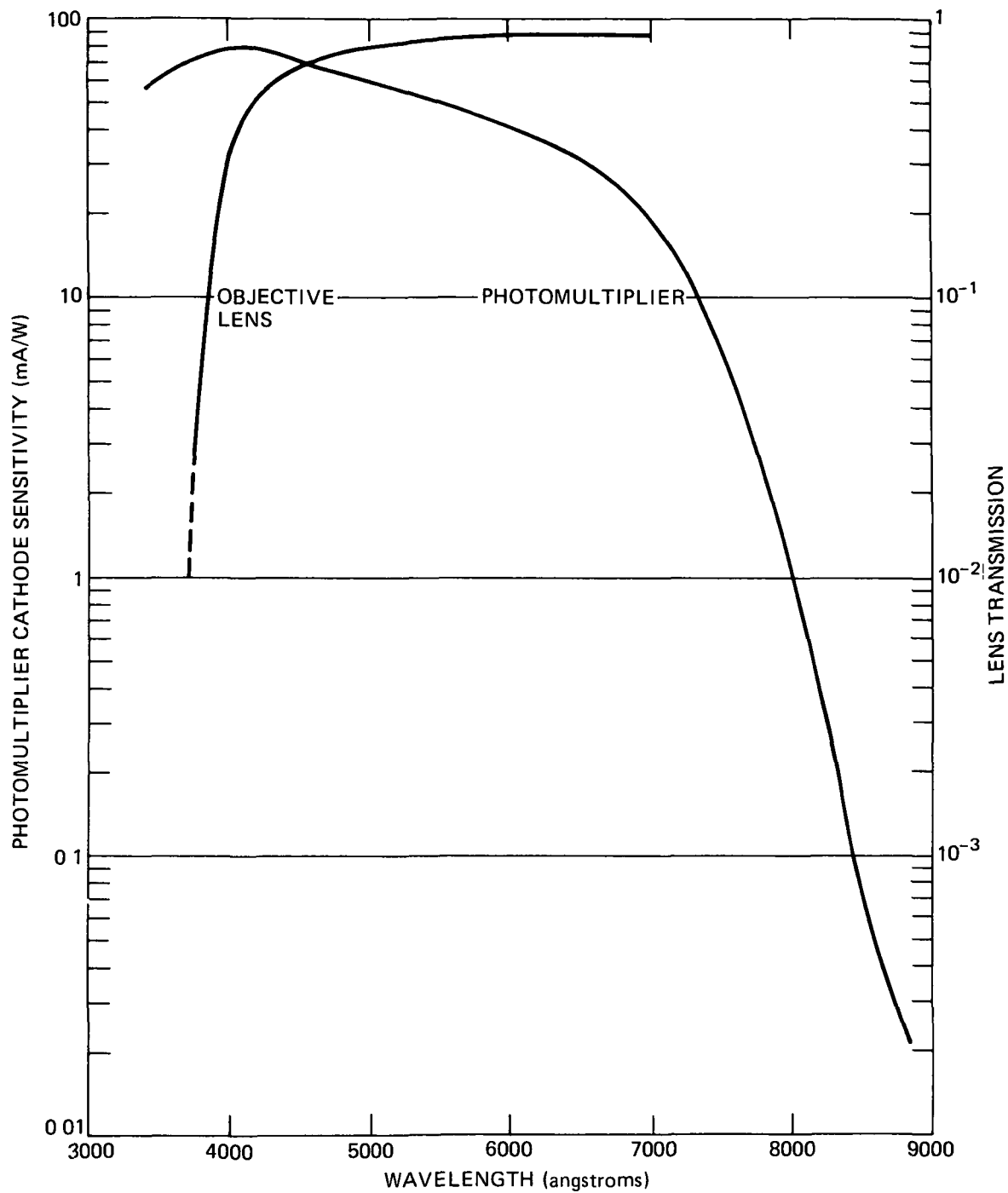
Fig 5 SPECTRAL CHARACTERISTIC OF PHOTOMULTIPLIER (S-20) AND
OBJECTIVE OPTIC
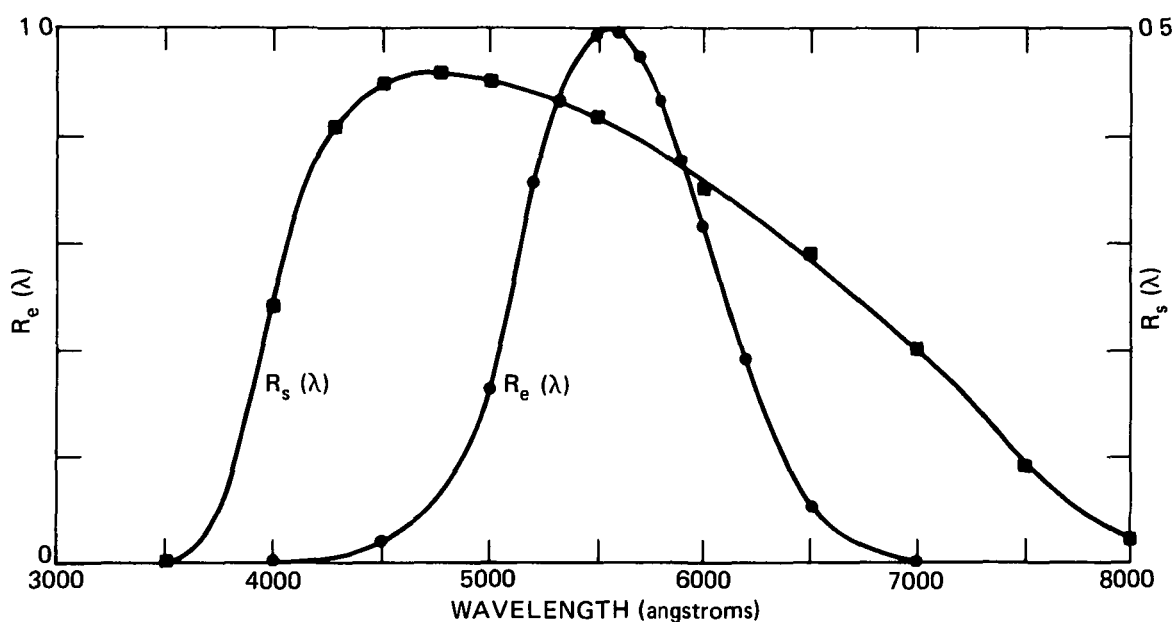
Fig 6 SPECTRAL CHARACTERISTIC OF STAR SENSOR AND THE EYE
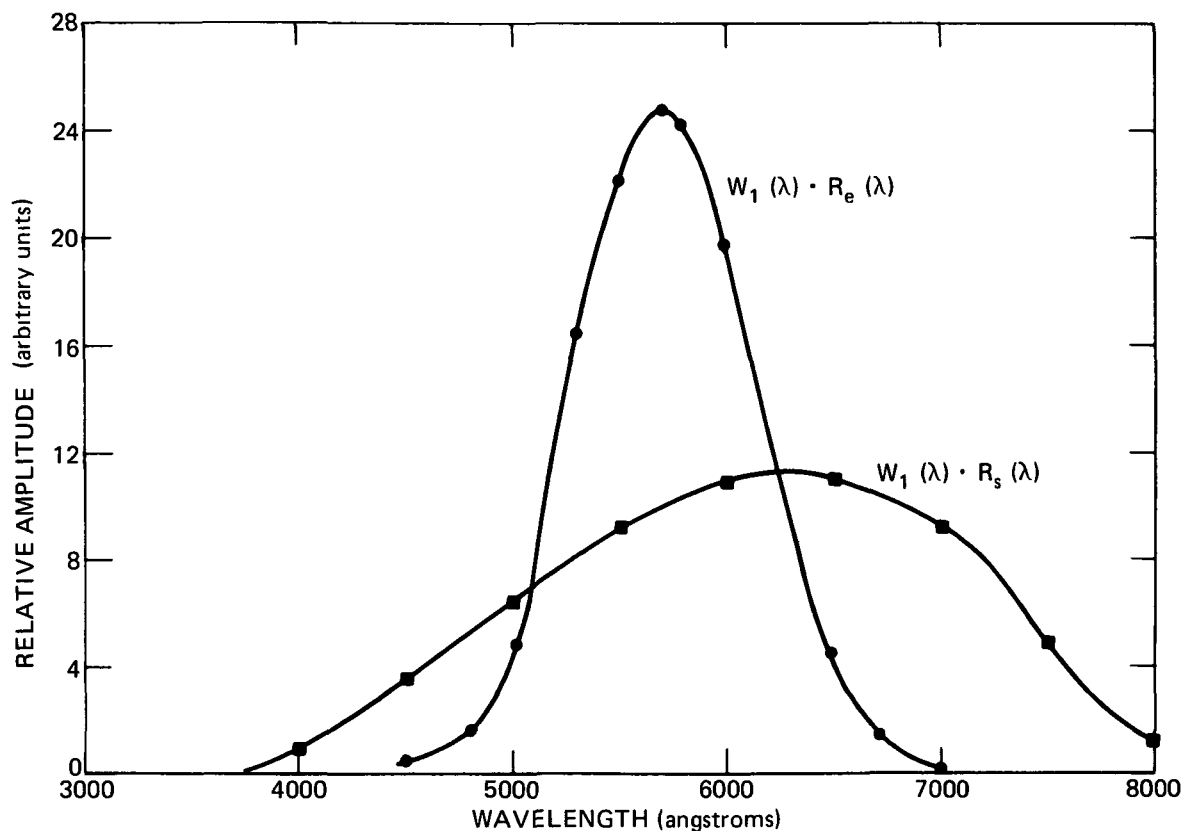
Fig 7 SPECTRAL CONVOLUTION OF 2870 °K SOURCE WITH THE STAR SENSOR
AND THE EYE
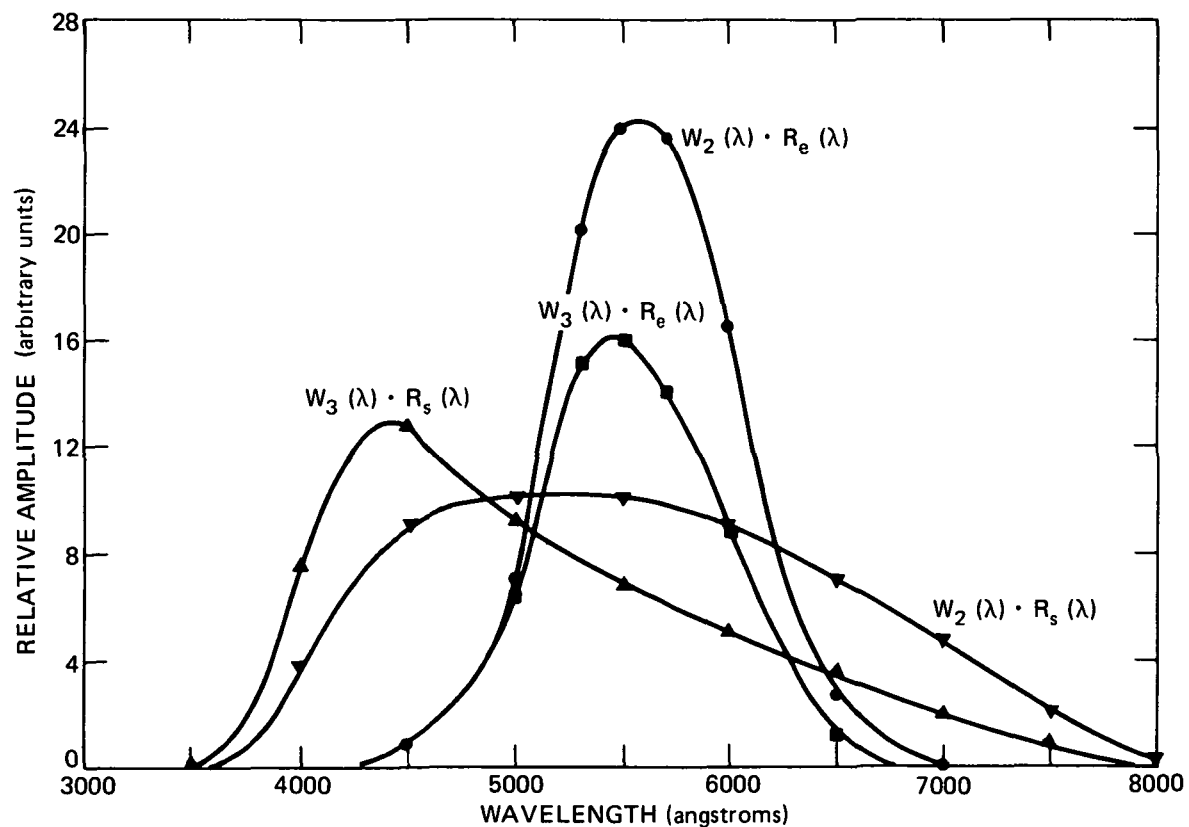
Fig 8 SPECTRAL CONVOLUTIONS OF A0 AND K0 STARS WITH THE STAR SENSOR
AND THE EYE

Therefore the sensor's response to a K0 source relative to a 2870°K source is·

$$\frac{841}{874} \times \frac{770}{776} = 0.955.$$

Response to A0 Star. The effective temperature of an A0 is 10 700°K. Multiplying the A0 curve, $W_3(\lambda)$, by the responses R_e and R_s, we obtain the products shown in Fig. 8. The areas under these two curves are

$$\int W_3(\lambda) \ R_e(\lambda) = 506,$$

$$\int W_3(\lambda) \ R_s(\lambda) = 711.$$

Therefore the sensor's response to an A0 source relative to a 2870°K source is

$$\frac{711}{874} \times \frac{770}{506} = 1.24.$$

By performing the indicated computations, it can be shown that the sensor's response to an A0 star relative to its response to a K0 star is 1.30. This ratio corresponds to a change in star magnitude of 0.3. Hence, given two stars of types A0 and K0 with equal visual magnitudes, the sensor's output will indicate a difference of 0.3 magnitude. Similarly, the sensor's response to a K0 source relative to a 2870°K source is computed as 0.955.

Photometry

The effective irradiance from a star as seen by a standard observer may be readily computed from the following formula·

$$I = I_o (2.51)^{-m_v} \ W/cm^2, \tag{5}$$

where

$$I_o = W/cm^2 \text{ (for a 0 visual magnitude A0 star,}$$
$$I_o = 3.1 \times 10^{-13} \ W/cm^2),$$
$$m_v = \text{visual magnitude } (\pm).$$

The total available effective power, P, from the star that is intercepted and passed through the lens is given by:

$$P = \frac{2.43 \times 10^{-13} \beta D_o^2}{(2.51)^{m_v}} \ watt, \tag{6}$$

where

$$\beta = \text{optic efficiency,}$$

$$D_o = \text{optic diameter in centimeters.}$$

Based upon the use of an optic with a 2-inch (5-cm) aperture and an efficiency, β, of 0.65, and an A0 star of +4 visual magnitude, the value for P is computed to be 9.90×10^{-14} watt.

In terms of radiant power, the irradiance from a 0 visual magnitude A0 star is·

$$H_o = 3.94 \times 10^{-12} \ W/cm^2.$$

For a +4 visual magnitude A0 star, the irradiance is $9.85 \times 10^{-14} \ W/cm^2$.

Background Effects

Stellar. The energy received from the background caused by stellar radiation will vary greatly with the region

of the heavens included in the field of view of the sensor. The mean sky brightness, N_T, resulting from 105 stars of +10 visual magnitude is 4.7 x 10^{-14} W/cm^2/deg^2. With the exception of the Milky Way, typical background radiance contours would include 50 stars of +10 visual magnitude.

When viewing the stellar background through the "N" shaped slit reticle, a solid angle of 1.6 deg^2 is enclosed, yielding a background of 7.52 x 10^{-14} W/cm^2. The background irradiance incident on the sensor is now only a function of the optical aperture.

Lunar. The radiation from the moon will become bothersome only when the star sensor is to function in its vicinity. The lunar illumination at the Earth's surface is 3 x 10^{-2} footcandle (fc) for a full moon. This corresponds to an effective irradiance of 4.4 x 10^{-8} W/cm^2. These values are not going to change significantly for a low-altitude satellite. The light shield will be capable of adequate discrimination against the lunar background to within several degrees of the edge of the star sensor field of view.

Exposure Protection

For the star sensor to operate properly, a light shield must be provided to permit operation to within 60° of the sun. While the star mapper is passing through a high-irradiance dead zone, the photomultiplier sensor must be protected against damage from excessive photocathode current drain. There are two possible ways to handle this situation. One is to provide a mechanical shutter that cuts off the illumination of the photomultiplier, the other is to permit this illumination of the photomultiplier while gating the photomultiplier high-voltage power supply to avoid excessive photocathode current drain. High photocathode current density will result in sensor damage. It is also essential, however, that the photocathode should not attain an excessive temperature as a result of solar illumination. As will be seen in a later section on sensor optics, the input irradiance to the star mapper is never focused to a small point on the sensor photocathode, which might cause

local hot-spot generation. For weight-reduction purposes and for improved general reliability, we have decided to avoid the use of a mechanical shutter.

The illumination sensor, as illustrated in Fig. 9, detects excessive irradiance and causes the photomultiplier high-voltage power supply to be turned off when this condition exists. The illumination sensor and its operation are discussed further in a later section.

Extensive tests have been performed to determine the effect of heating on the star mapper components when it is operated without a shutter and with full solar exposure. The two components of interest are the "N" slit reticle, upon which all input signals are focused, and the photomultiplier window, upon which the photosensitive cathode is formed. The tests consisted of instrumenting a complete optical train with a thermocouple on the "N" slit reticle and another thermocouple on a gray-body absorber that was placed in position in lieu of the photomultiplier. The entrance aperture of the objective optic was illuminated by means of a collimated carbon arc source equivalent to one or more suns. The carbon arc source output was continuously monitored by a silicon solar cell. These tests were performed in a vacuum chamber with a pressure of 10^{-5} Torr. The results of the tests are shown in Fig. 10. Note that the temperature of the photomultiplier simulated window rose to 120°F (47°C), which is below the permissible limit of 65°C for the photocathode. The quartz reticle plate approached 150°F, which is of no consequence even for the thin-film aluminum reticle coating. It should be remembered that these tests indicated what might happen should the satellite discontinue spinning with the star mapper continuously viewing the sun. An additional test was performed with the instrument viewing the sun. In general the results so obtained were in good agreement with the thermal vacuum tests.

WINDOW, 0 200′ THICK

LENS, 7MM FOCAL LENGTH 5 MM DIA

FILTER

SOLAR CELL

HOUSING

LENS RETAINER

SOLAR CELL RETAINER

WASHER

INSERT

ECCOFOAM

A-A

SILICONE RUBBER

GLYPTAL

30 MAX TWIST

NYLON PIN

B-B

A

B

B

A
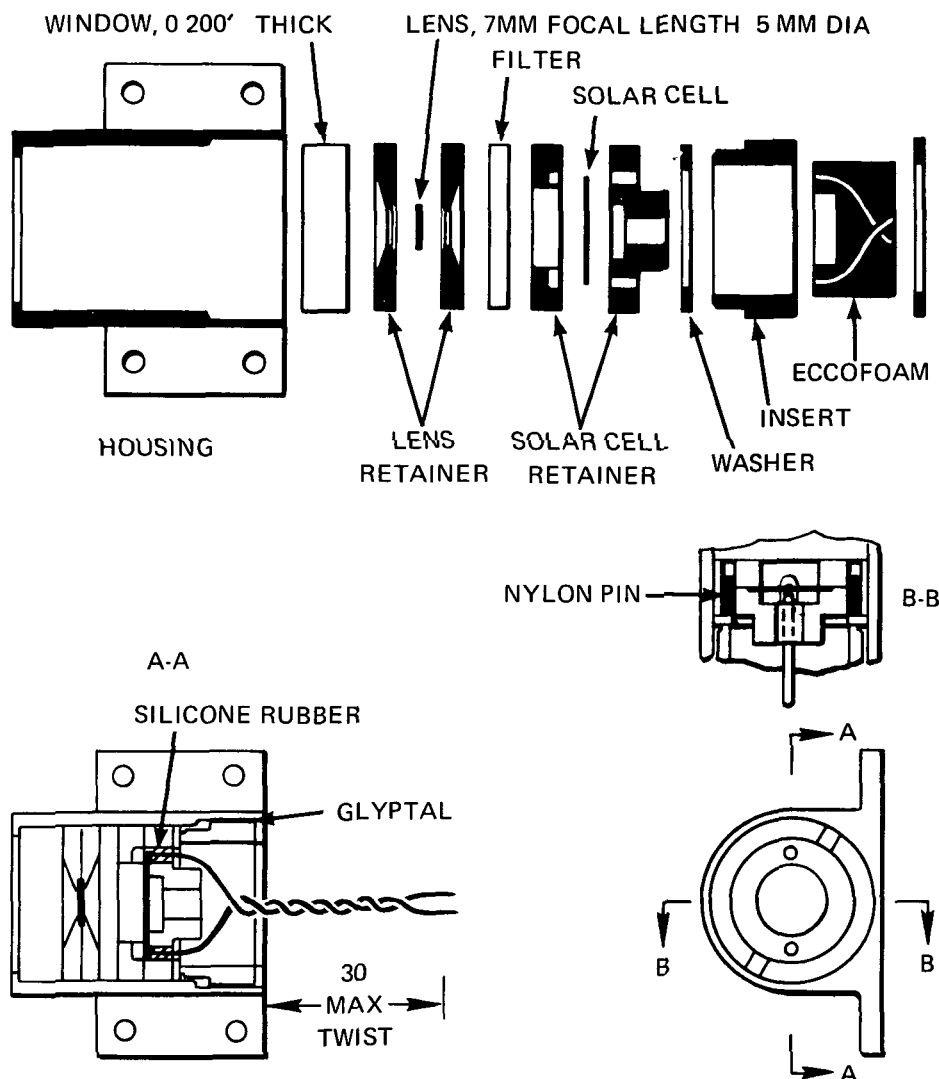
Fig 9   ILLUMINATION SENSOR COMPONENT LAYOUT
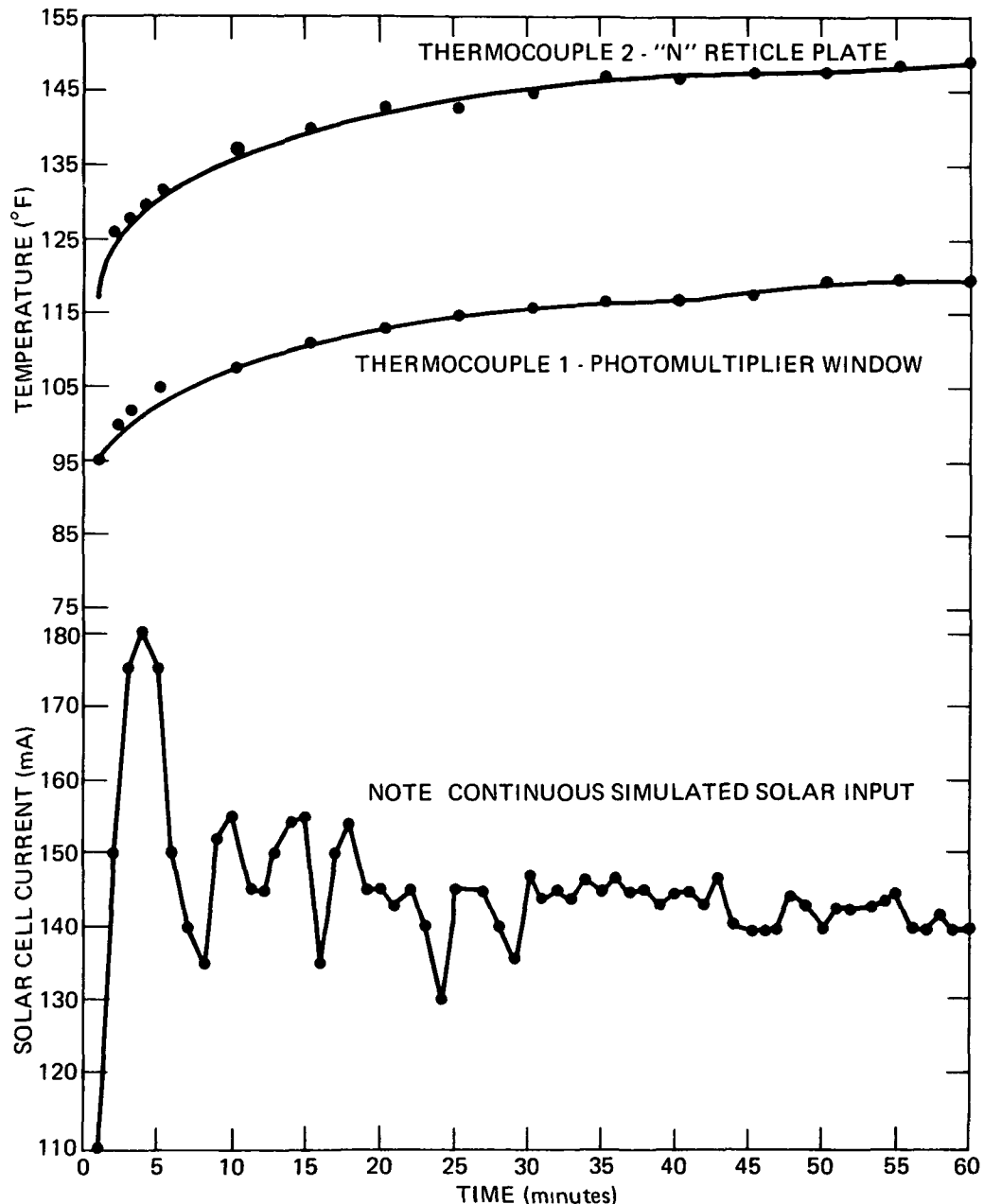
Fig 10   PLOT OF OPTICAL COMPONENT TEMPERATURES WITH SIMULATED
SOLAR ILLUMINATION

OPTICS

Objective

The optics of the star sensor must be both rugged and reasonably light weight. The focal length is determined by the desired size of the image format, which in this case is the "N" shaped slit. The optical aperture is determined on the basis of required signal strength to yield an acceptable signal-to-noise ratio at the detector.

Using a 4-inch focal length, f/2 Super Baltar optic with a transmission, β, of 0.65, an A0 star of +4 visual magnitude will yield an input luminous flux at the detector (assuming no loss in the condenser optic) of 9.90×10^{-14} watt.

Condenser Optics (Field Lens)

The express purpose of including a small condenser/ field optic behind the "N" slit (Fig. 3) is to converge light rays, caused by a star image anywhere on the "N" slit, to a common-limit circular area on the detector. This feature is very important when we are attempting to differentiate between various star signal amplitudes. It is not in the least unusual for a sensor to have a ±20% variation in sensitivity when a plot is taken across its photosensitive area. The condenser/field optic overcomes this problem by ensuring that the same area of the sensor photosurface is used at all times, independent of the location of the star on the "N" slit. The condenser optic takes the form of two double convex lenses, 29 mm in diameter and with a focal length of 26 mm.

To ensure capture of all the rays exiting from the objective optic, the condenser/field optic forms a minified image of the exit aperture of the objective onto an area of predetermined size on the photomultiplier. The ratio of the diameters of the objective exit to the spot on the photomultiplier is the condenser magnification. The diameter of the condenser/field lens is adequate to avoid ray vignetting.

Figure 11 illustrates the condenser/field lens arrangement. The double condenser was used to obtain a short effective focal length with a large aperture. The parameters of the condenser/field lens design are· D_2 = 90 mm = 3.54 inches, f = 13 mm, D_1 = 15.2 mm = 0.598 inch, and the magnification M = 5.92. The exit aperture of the 4-inch Super Baltar lens is 1.5 inches in diameter.

Design of "N" Shaped Slit Reticle

The "N" slit must be held rigid in the focal plane of the objective optic. To accomplish this, the "N" shaped slit reticle is formed on a quartz plate that is coated with a vacuum-deposited precision aluminum film, to yield a transparent slit in an opaque field. The quartz plate containing the slit is then mounted in an integral unit with the condensing optic as shown in Fig. 12. It can be seen from Fig. 12 that the objective optic, folding mirror, and reticle-condenser assembly are rigidly mounted in a common frame. The mounting of the photomultiplier tube is less critical, since it collects unfocused energy.

PHOTOMULTIPLIER SENSOR

The signal sensing element for this system is a highly sensitive, high-gain, ruggedized photomultiplier. The S-20 spectral sensitivity of the photomultiplier tube is between 300 and 600 millimicrons. The secondary electron amplification is of the order of 10^6. It is important for the tube to have a low anode dark current, the major portion of which is attributable to photocathode thermionic electron emission. A type EMR 541E-01-14 tube was selected for this application. This tube has a typical photocathode sensitivity of 185 μA/lumen, a gain of 10^6, and an anode noise equivalent input of 1.6×10^{-11} lumen. Figure 13 shows the integral photomultiplier/high-voltage power supply.

STAR SIGNAL DETECTION

Signal-to-noise ratios have been determined based on calculations and laboratory tests. These results will

$$M = A/B \quad D_1 = f(1 + 1/M) \quad D_2 = f(1 + M)$$

$$f_{\text{CONDENSER SYSTEM}} = F/(2F-S)$$

F = INDIVIDUAL FOCAL LENGTH

S = SEPARATION OF LENS PAIR
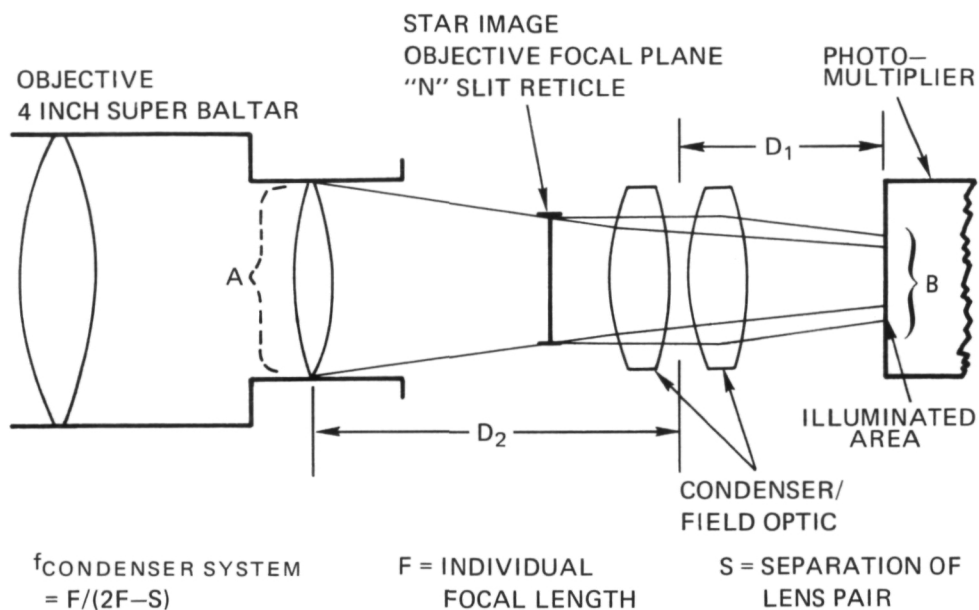
Fig. 11   CONDENSER/FIELD OPTICS
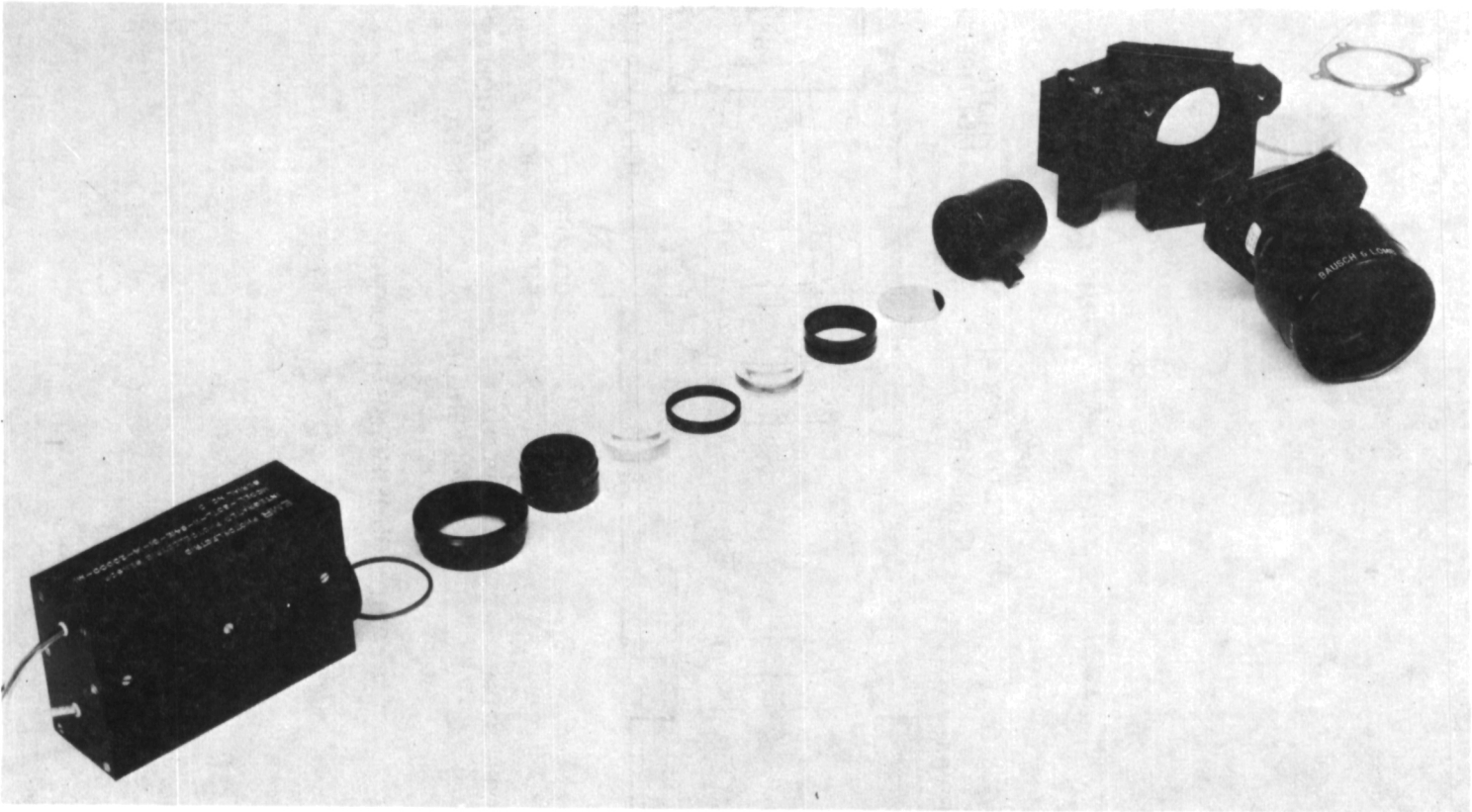
Fig. 12   OPTICAL TRAIN COMPONENTS

THE JOHNS HOPKINS UNIVERSITY
APPLIED PHYSICS LABORATORY
SILVER SPRING. MARYLAND
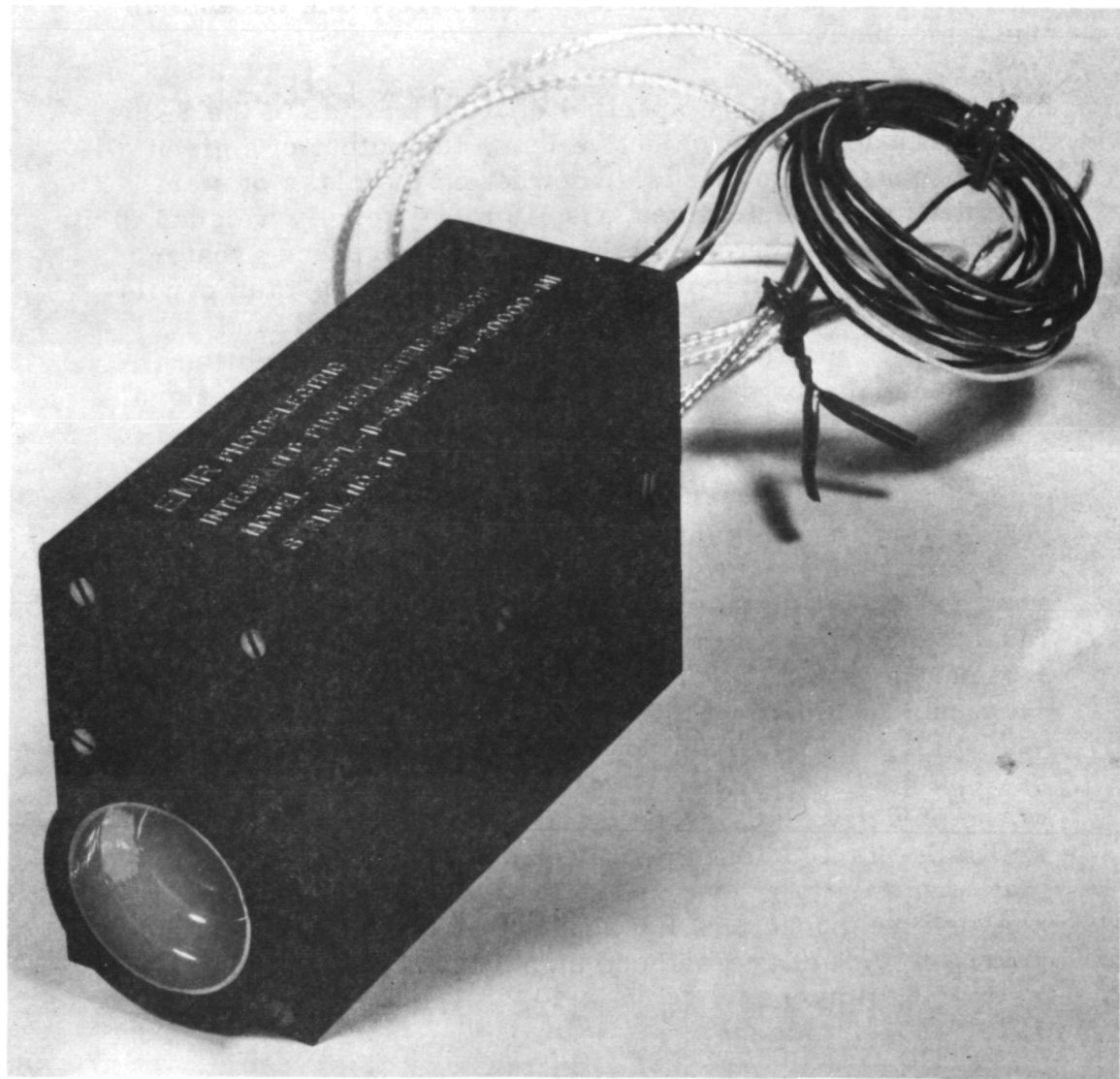
Fig. 13   INTEGRAL PMT AND HIGH-VOLTAGE POWER SUPPLY

be compared to results obtained in the field. A perfect
simulation of orbital conditions cannot be made because of
the atmosphere.

Because of the spectral characteristics of the S-20
photocathode and the objective lens, the output of a given
visual magnitude depends somewhat on the class of star.
The sensor's spectral response is more heavily weighed in
the blue than is the eye so that hot stars produce greater
outputs than cool stars. An examination of the star popula-
tion shows a spread primarily between types B and K,
with the A and K most predominant. The population
drops sharply for stars cooler than type K. Hence, signal-
to-noise ratios will be computed for the K0 type, consid-
ered now as a worst case.

For the combination of optics and sensor discussed
in the preceding paragraphs, the photocathode signal cur-
rent can be estimated quickly. The effective radiant power
(as seen by a standard observer) from a +4 visual magnitude
K0 star is exactly equal to the effective radiant power of a
+4 visual magnitude A0 star by virtue of the definition of
visual magnitude. This power has been previously computed
as 9.90×10^{-14} watt, neglecting the spectral characteristic
of the objective lens. The cathode sensitivity of the photo-
multiplier is 185 μA/lumen for a 2870°K source. Noting
that, from the previous spectral computations, the star
sensor's response to a K0 source relative to a 2870°K
source is 0.955, the cathode signal level is then 9.90×10^{-14}
watt $\times$ 680 lumens/W $\times$ 185 $\times 10^{-6}$ A/lumen $\times$ 0.955 =
1.19×10^{-14} ampere.

The photocathode signal may also be determined
based on a field calibration. The peak signal level follow-
ing the bandpass filter in response to a +4 visual magnitude
K0 star is 47 mV. The transresistance gain of the band-
pass amplifier in response to a pulse is $2 \times 1.96 \times 10^{6} \times$
$0.775 = 3.04 \times 10^{6}$. (The factor 0.775 is a result of the
bandpass filter's effect upon a rectangular pulse.) There-
fore the +4 visual magnitude (K0) amplifier level of 47 mV
is encountered with an anode current of 1.54×10^{-8} ampere.

The photomultiplier's gain is 1.9×10^6, as per the gain characteristic curve. Hence the signal level at the cathode is 8.15×10^{-15} ampere. The difference between the above calculated and measured photocathode signal levels may be attributed to the slight variance in the photomultiplier gain, variance in atmospheric attenuation, and neglect of the spectral effect of the lens upon a 2870°K source.

The sky background will contribute a typical total radiance, N_T, of 4.7×10^{-14} W/cm^2/deg^2, with a spectral distribution approximating that of an A0 star. The slit at the reticle encompasses 1.6 deg^2. Hence the background irradiance is 7.5×10^{-14} W/cm^2.

The total irradiance of a 0 magnitude A0 star is given as $H_o = 3.94 \times 10^{-12}$ W/cm^2. For a fourth magnitude star (a factor of 40 weaker), the total irradiance is 0.99×10^{-13} W/cm^2. Both N_T given above and H_o represent total power density and are not corrected for the sensor spectral characteristic.

Any spectral filtering performed by the optics and the photocathode is applied equally to both of these inputs. Hence, at the photocathode the ratio of background current to signal current from a +4 visual magnitude A0 star must remain 0.75.

As described in a previous section, the sensor's response to an A0 star is calculated to be 1.30 times its response to a K0 star. The ratio of background current to that of a +4 visual magnitude K0 star is then $0.75 \times 1.30 = 0.98$. The background current is therefore $0.98 \times 8.15 \times 10^{-15} = 8.00 \times 10^{-15}$ ampere. Although this background current is comparable to the signal level, it is DC, whereas the star signal is a pulse. Nevertheless, the presence of this DC background signal results in noise. The noise associated with any signal current, i, is given by the shot current equation:

$$\overline{i}_N = (2ei\ \Delta f)^{\frac{1}{2}}, \tag{7}$$

where

e = electronic charge = 1.6×10^{-19} couloumb,

Δf = noise bandwidth = $1.57 \times$ 3-dB bandwidth.

For the 1/12 rpm spin rate, where the 3-dB bandwidth is 9 Hz, the rms noise resulting from the stellar background, $\bar{i}_{NSSB}$, is computed from Eq. (7):

$$i_{SSB} = 8.00 \times 10^{-15} \text{ ampere.}$$

$$\bar{i}_{NSSB} = 1.90 \times 10^{-16} \text{ ampere.}$$

The rms noise resulting from the thermionic electron emission, $\bar{i}_{NST}$, within the photomultiplier sensor may also be computed by substituting into Eq. (7), where:

$$i_{STherm} = 2.96 \times 10^{-15} \text{ ampere.}$$

$$\bar{i}_{NST} = 1.16 \times 10^{-16} \text{ ampere.}$$

The noise in the signal $\bar{i}_{NS}$ caused by the presence of a K0 star of +4 visual magnitude, when computed from Eq. (7), is:

$$i_S = 8.15 \times 10^{-15} \text{ ampere.}$$

$$\bar{i}_{NS} = 1.92 \times 10^{-16} \text{ ampere.}$$

The total noise current may be expressed as:

$$\bar{i}_{NT} = \left(\bar{i}_{NS}^{2} + \bar{i}_{NST}^{2} + \bar{i}_{NSSB}^{2} \right)^{\frac{1}{2}} \text{ ampere.} \qquad (8)$$

$$\bar{i}_{NT} = 2.94 \times 10^{-16} \text{ ampere.}$$

It is apparent that the noise contribution from the stellar background is significant in this case.

Because of the electrical bandpass filter characteristic, the signal to which the peak detectors charge is 0.775 times the input signal. The signal-to-noise ratio based on the measured signal from a K0 star is therefore:

$$\frac{S}{N} = \frac{0.775 \times 8.15 \times 10^{-15}}{2.94 \times 10^{-16}} = 21.5 \approx 26.6 \text{ dB.}$$

In the fast mode, the bandwidth is expanded by a factor of 12, thereby reducing signal-to-noise ratios by $\sqrt{12}$:

$$\overline{i}_{NT} = 1.02 \times 10^{-15} \text{ ampere.}$$

$$\frac{S}{N} = 6.20 \text{ or } 15.8 \text{ dB.}$$

(Note: Except for the high-temperature extreme, the particular phototubes used exhibit far less dark current than the specified volume.)

For the purpose of making false alarm calculations, it is convenient to refer to signal-to-noise ratios where the noise is that present in the absence of a star. Performing the foregoing calculations, but with no noise contribution from the star signal, the following ratios are obtained:

$$\frac{S}{N} = 28.4 = 29.1 \text{ dB (slow mode),}$$

$$\frac{S}{N} = 8.20 = 18.3 \text{ dB (fast mode).}$$

It should be stressed that these are signal-to-noise ratios when there is no noise contribution from the sun. Although, the low-frequency blocking will greatly attenuate the sun signal, the shot noise associated with the sun current may still add significantly to the total noise. A sun signal equal to a fourth magnitude star would reduce the signal-to-noise ratios about 3 dB in the absence of signal and about 1.8 dB in the presence of signal. For a sun signal equivalent to a second magnitude star, the deterioration would be more serious: 8.7 dB in the absence of signal, and 6.2 dB in the presence of signal.

The value used for sky background is an overall average (105 tenth magnitude stars per square degree). Most of the time, the background intensity contribution is lower, equivalent to about 50 stars per square degree, but there are also small areas of the Milky Way where the background increases to six or seven times the average. Here, too, the signal-to-noise ratios will deteriorate up to 9 dB.

An analysis of detection and false alarm probability is given in Appendix B. This analysis is predicated upon the signal-to-noise ratios calculated above for the fast spin mode of satellite operation.

SIGNAL PROCESSING

Solar Response

Photomultiplier dark current and current caused by sky background are significant relative to fourth magnitude star levels, so that the need to block direct current is obvious. But in addition, there may be a fairly large sun signal resulting in a triangular waveform caused by the spinning of the satellite. This signal can be attenuated according to the low-frequency corner used to block the direct current. For the case of the optic axis cutting across the sun, the photomultiplier current waveform will be approximately as shown in Fig. 14a. At the slow spin rate, assuming photomultiplier switching at 53° from the sun, τ = 74 seconds.
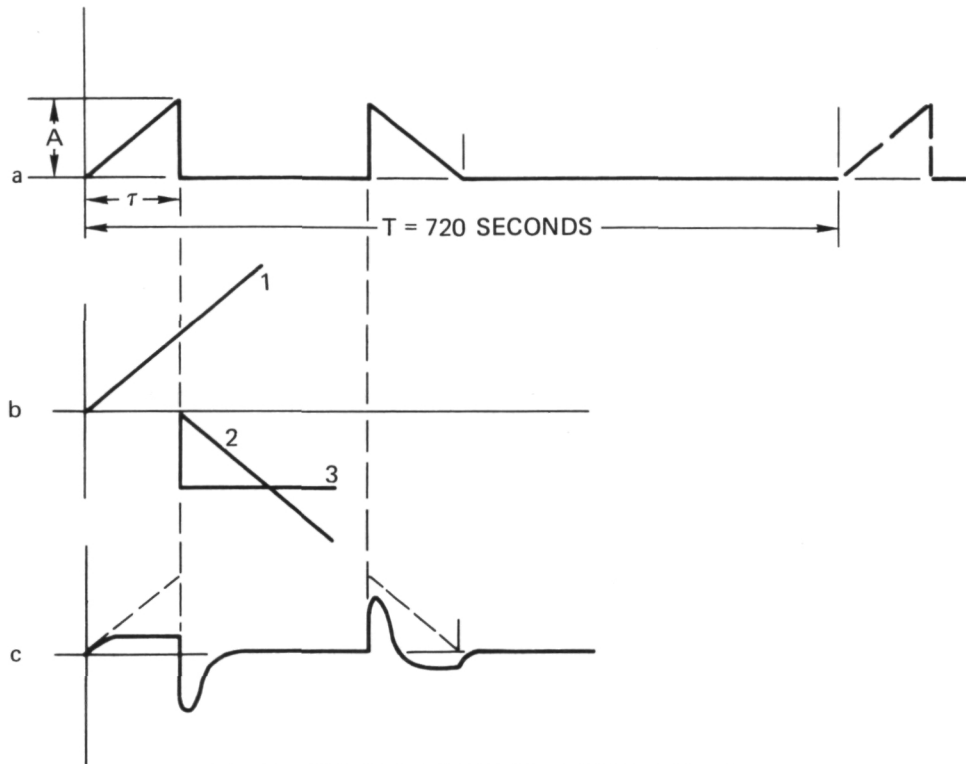
Fig. 14   STAR SENSOR SOLAR WAVEFORM

This waveform can be broken down into the sum of ramps and steps (Fig. 14b). With no DC blocking, the interfering Sun signal approaches the amplitude, A. Using a bandpass filter with a lower corner, ω_L, and an upper corner, ω_H, the output in response to a ramp is:

$$E(s) = \frac{A}{\tau s^2} \frac{\omega_H s}{(s + \omega_H)(s + \omega_L)} . \tag{9}$$

The final value of e(t) is $A/\tau\omega_L$. Hence the ramp peak is reduced by a factor of $1/\tau\omega_L$. A choice of a 1-Hz corner $(\omega_L = 6.28)$ will produce a considerable sun signal attenuation without excessive reduction of the star signal peak.

The response to the composite waveform is shown in Fig. 14c. The sharp negative peak spills over into the off period. The positive peak can interfere with subsequent star signals, while decaying with a time constant of $1/\omega_L$. Allowing a full 10 time constants for complete decay, there is a possible interference with star sensing for less than 2 seconds following turnon. In terms of angular rotation, this is less than 1°. The inoperative period in the fast mode is unchanged in terms of angle, since the low corner frequency is scaled upward proportional to the spin rate.

Stellar Response

For a bandpass filter with $\omega_H = 62.8$ and $\omega_L = 6.28$, the response to a unit step is:

$$E(s) = \frac{1}{s} \cdot \frac{62.8s}{(s + 62.8)(s + 6.28)} . \tag{10}$$

$$e(t) = 1.11 \left(\epsilon^{-6.28t} - \epsilon^{-62.8t} \right). \tag{11}$$

This waveform peaks at t = 0.0407, at which time e = 0.775. This is the signal value to which the peak detectors will charge. In practice, the incoming star signal

departs from a rectangular waveform because of the finite star image at the slit. The actual peak is then somewhat reduced from the value calculated here. At the filter output, the star waveform appears as in Fig. 15.

SIGNAL PROCESSING ELECTRONICS

General Description

The overall functioning of the star sensor can be seen in the block diagram (Fig. 16) with the aid of the timing diagram (Fig. 17).

To review briefly, the star sensor's function is to provide star intensity data to the telemetry with an angular resolution of 3 arc minutes. This resolution is given by the slit widths in a reticle placed in the optical focal plane. At the nominal satellite spin rate of 1/12 rpm, a star causes a 100-ms pulse to be produced out of the photomultiplier. Telemetry sampling every 48 ms thus is sufficient to preserve the required resolution. However, with a spin rate of 1 rpm (backup mode), the star pulses are only 8.5 ms wide, and therefore a separate timing channel is required to preserve a resolution of 3 arc minutes. The amplitude channel must also contain a memory capability in the fast mode. Peak detection rather than integration is used for this memory so as not to add noise during the entire sampling interval (see Appendix C).

A dynamic range of 200 is presented by stars ranging from a fourth magnitude K0 to the brightest star (Sirius, -1.46 magnitude). The spacecraft telemetry requires a logarithmic compression of amplitude data prior to data acceptance. This cannot be done at an early stage without seriously deteriorating signal-to-noise ratios. A level of 47 mV at the linear amplifier is chosen for a +4 visual magnitude K0 star so that, with the sole exception of Sirius, no star exceeds saturation. Precision circuitry, essential to process signals of this level, requires a liberal use of operational amplifiers. Fortunately the availability
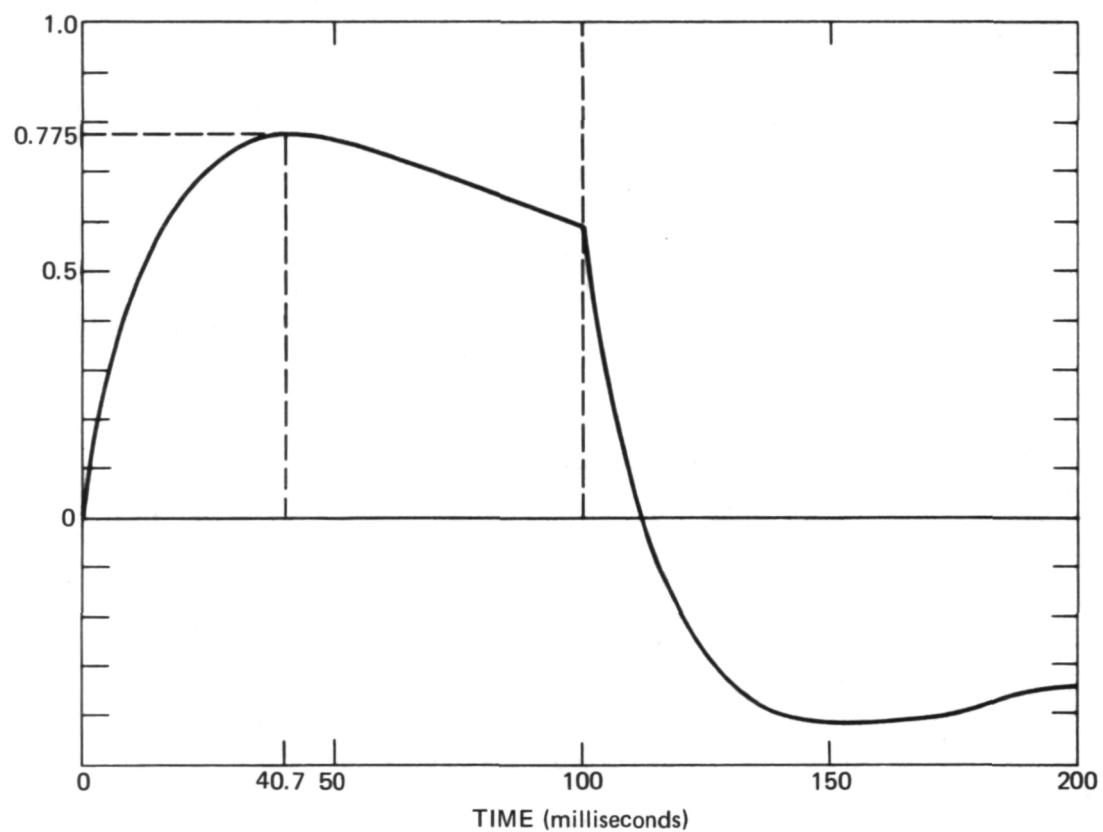
Fig. 15 STAR PULSE WAVEFORM AT FILTER OUTPUT
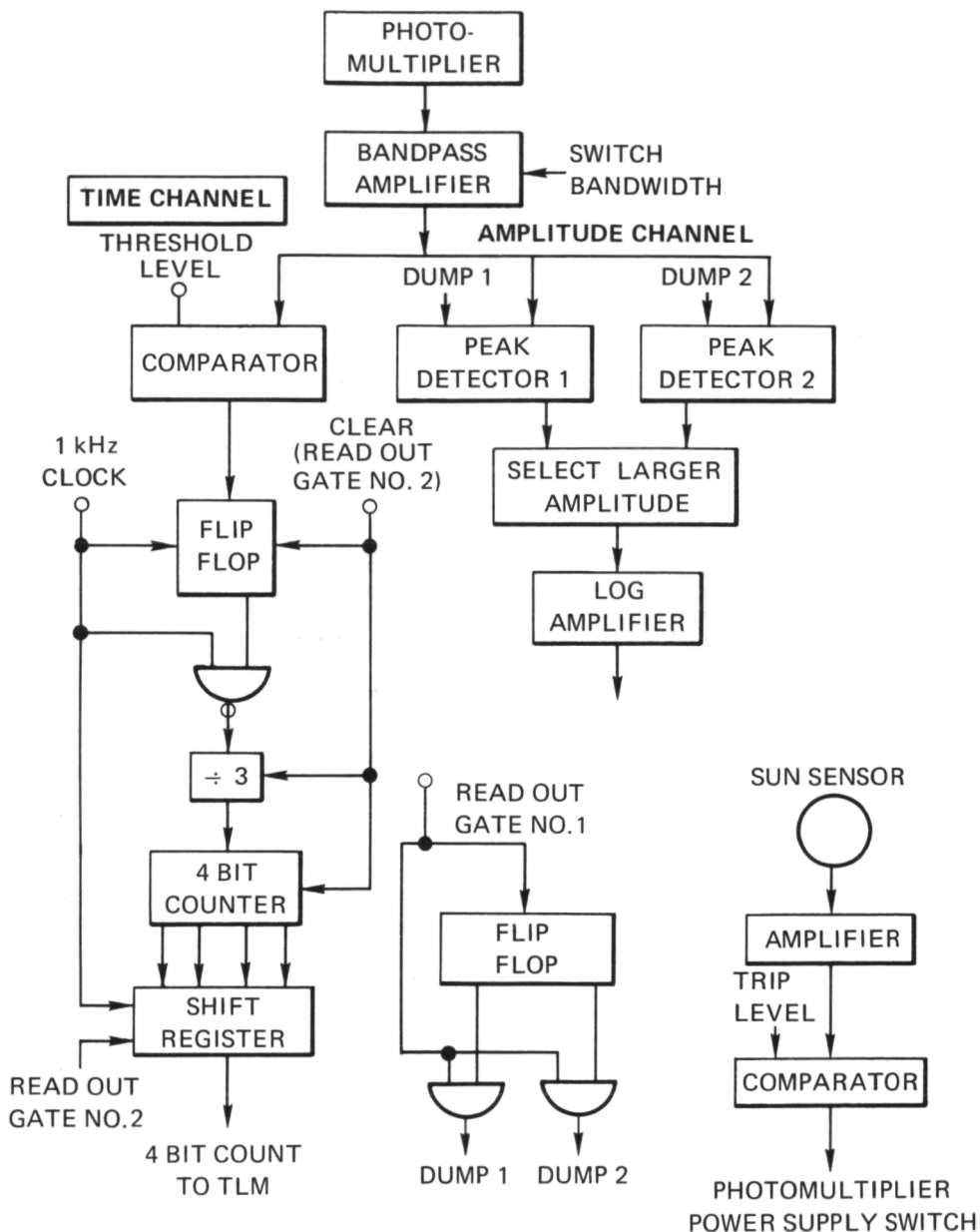
Fig. 16   BLOCK DIAGRAM OF STAR SENSOR ELECTRONICS
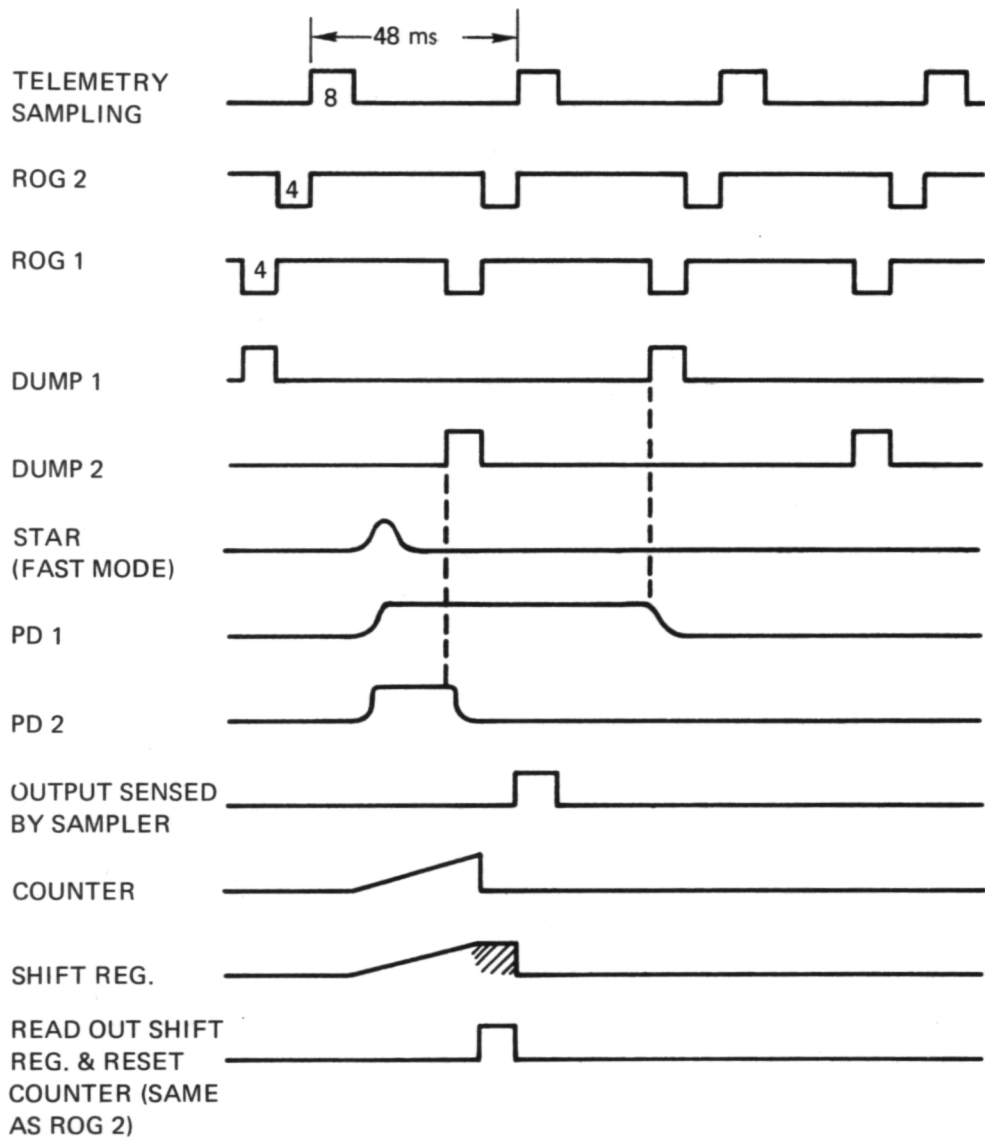
Fig. 17 TIMING DIAGRAM FOR STAR SENSOR FUNCTIONS

of a low-power operational amplifier such as the LM 108 (typical current drain from each of the supplies is 0.15 mA) permits compliance with the power budget.

The photomultiplier current pulse is amplified and converted to a voltage pulse with a peak of 47 mV for a fourth magnitude star. Bandpass filtering is used to give a bandwidth of approximately 1 to 10 Hz for the slow mode and 12 to 120 Hz for the fast mode, switchable upon command. The high-frequency corner filters out higher-frequency random noise, while the low-frequency corner is necessary to (a) block the DC component caused by sky background and photomultiplier dark current, and (b) attenuate the sun signal. These bandwidths are less than those required for good pulse fidelity, since maximizing the peak signal-to-noise ratio is more important. A further gain in signal-to-noise ratio can be obtained by further reducing the high-frequency corner. However, the following undesirable effects would become noticeable:

1. The timing channel resolution capability of 3 ms in the fast mode would be degraded because of the fixed level threshold detector.

2. Since peak amplitude would be achieved only toward the end of the pulse period, amplitude calibration would depend on precise slit width and precise spin rate.

The low-frequency corner is simply obtained by R-C coupling into a second-stage amplifier. This corner frequency is sufficiently high so that a significant undershoot with a long tail results. Following a strong signal, a wait of up to 11 star signal pulse widths is required before a weak star can be processed accurately. In the original design a precision clamper was contemplated to eliminate this effect; however, the probability of a weak star following so closely behind a strong one is insufficient to warrant acceptance of the increased noise level caused by a clamping circuit.

Available to the star sensor are a 1-kHz clock and two readout gates. Readout gate 2 is a 4-ms pulse

immediately preceding the sampling period; readout gate 1 is a 4-ms pulse immediately preceding gate 2 (see timing diagram, Fig. 17).

Proceeding now with the amplitude channel, two parallel peak detectors are used. These detectors are discharged on alternate ROG-1 pulses. The alternate dump pulses are generated at one-half the rate but in synchronism with the ROG-1 readout gate. This arrangement guarantees that, in the fast mode, at least one detector will charge to the star signal peak, regardless of its time of occurrence. With a single peak detector, regardless of the choice of timing of the dump pulse, there is always a possible time of occurrence of a star pulse that would result in an incorrect reading (because of the width of the telemetry sampling period). Note that the selection of alternate ROG-1 pulses as dump pulses allows some 4 ms before the start of the sampling period; if a star pulse is early enough to incorrectly charge one of the peak detectors, it is also early enough to correctly charge the second detector prior to sampling.

Following the peak detectors is a selector stage that reads the larger of the two peak detector outputs for presentation to the log amplifier.

The log amplifier compresses the amplitude range so that weak stars can be satisfactorily read by the telemetry. Since star magnitude is also the logarithm of star intensity, the output of the log amplifier is a linear function of star magnitude. A scale factor of 1.54 volts per star magnitude is chosen. The amplifier is adjusted so that a fourth magnitude K0 star produces an output of -3.2 volts, well above the lower telemetry limit of -5 volts. All bright stars produce an output less than the +5 volt telemetry saturation level, with the sole exception of Sirius. The log amplifier is temperature-compensated both for slope and offset.

In the slow mode, no timing information is needed beyond that given by a telemetry sample. The required 3

arc minutes of resolution are equivalent to the 100-ms
star pulse width. In the fast mode, the 3 arc minutes are
equivalent to the narrower 8.5-ms pulse width. The ampli-
tude channel with its 48-ms sampling period must be sup-
plemented with an additional timing channel.

In the timing channel, a star pulse is detected by a
comparator whenever a fixed threshold is exceeded. The
timing channel's function is to develop a count that will
indicate elapsed time between the occurrence of the star
pulse and ROG-2. When the star is detected, a 1-kHz
train of pulses is gated into the counter circuits. First,
a divide-by-3 circuit is used, making each output pulse
represent a 3-ms increment. These pulses are then counted
in a four-bit counter. The 48-ms sampling period is thus
divided into 16 possible counts, each representing 3 ms.
While counting up, the shift register keeps in step with the
counter until ROG-2 occurs. The last count in the register
is then read out serially by the next four clock pulses. At
the same time, the counters are cleared and made ready for
the next star pulse.

Protection is needed for the photomultiplier when the
star sensor is aimed in the vicinity of the sun. The ampli-
fied current from a sun sensor will trip a comparator when
the sun is within 53° of the line of sight. The comparator's
output is used to switch off the photomultiplier's power
supply.

Figure 18 shows one of the star mapper's circuit
boards. Figure 19 shows the star mapper opened up to
display the electronics and optical train.

Circuit Details

For the purpose of this discussion, the reader is
referred to the schematic in Fig. 20. Full amplification
of the star signal is achieved in the first two stages, U1
and U3. Photomultiplier anode current feeds directly into
the U1 inverting input. The feedback capacitor of U1 de-
termines the high-frequency corner. R4 and the photo-
multiplier gain are so selected that a fourth magnitude

- 39 -
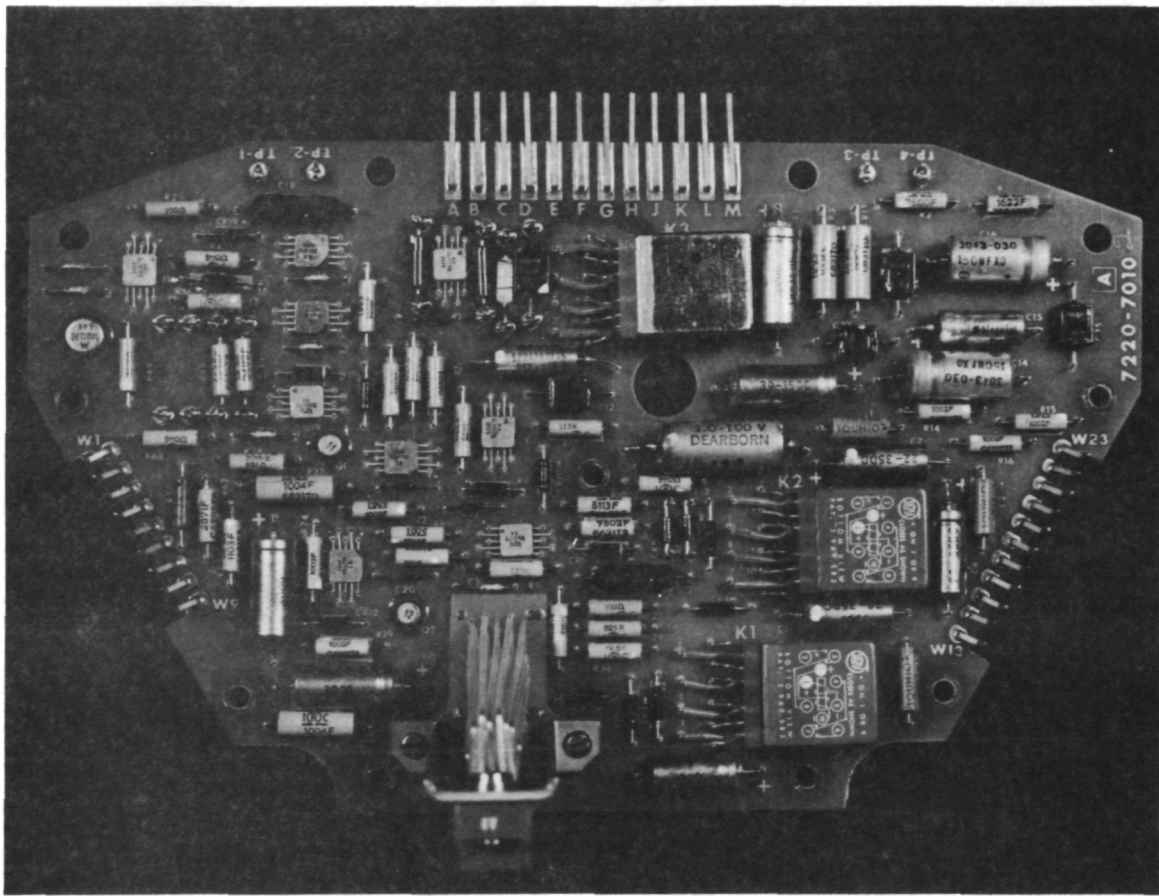
Fig. 18   STAR MAPPER CIRCUIT BOARD
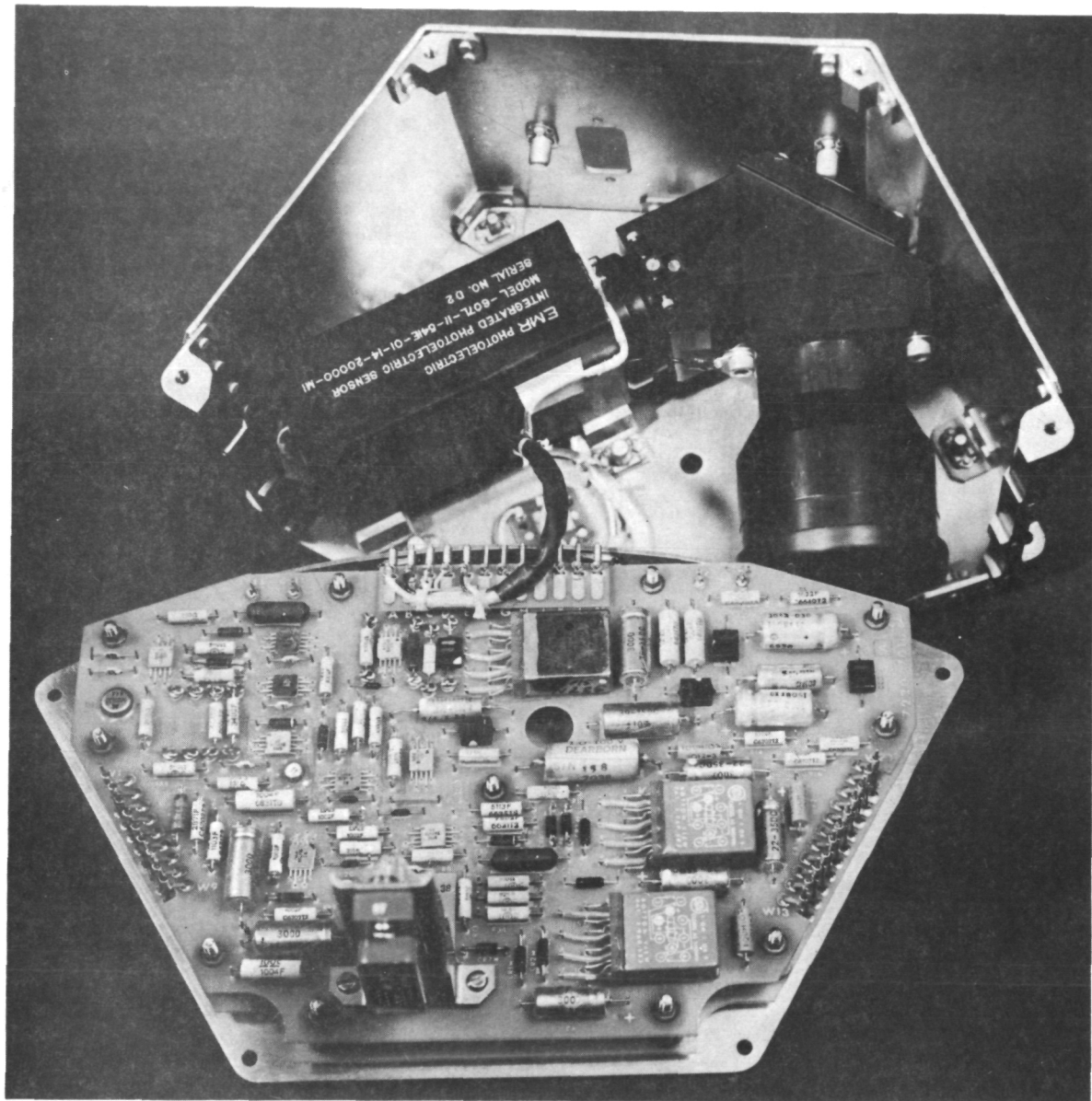
Fig. 19   STAR MAPPER INTERIOR

Page intentionally left blank
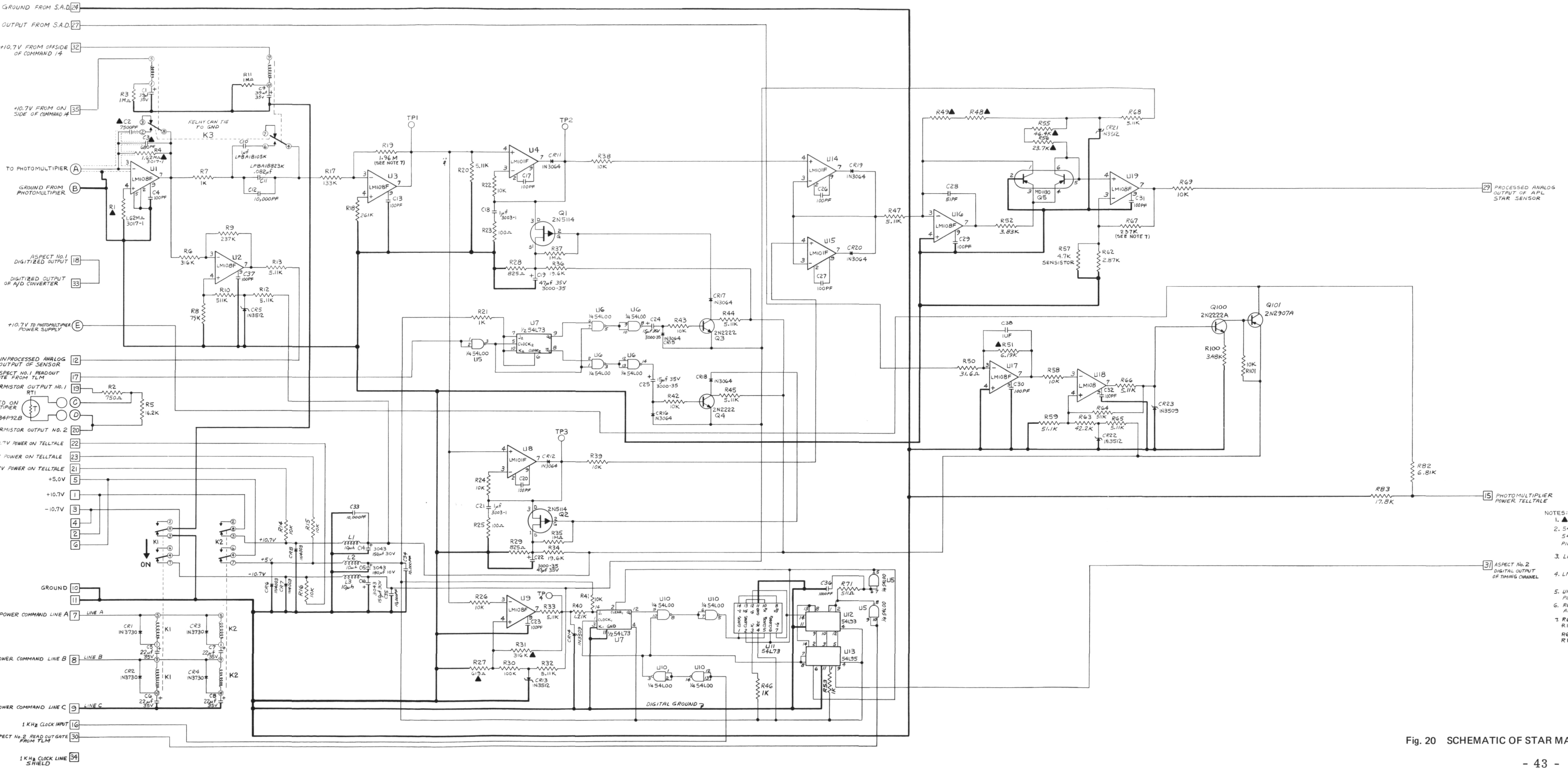
Fig. 20 SCHEMATIC OF STAR MAPPER ELECTRONICS

Page intentionally left blank

star develops a 47-mV peak at the output of U3. When bandwidths are switched, both the high and low corner frequencies are made proportional to the satellite spin rate, so that pulse shape and magnitude are preserved (but scaled in time), making the amplitude calibration independent of spin rate. A gain of 2 was designed into U3 so that a large sun signal would have to be added to a bright star before saturation could occur in U1. Although the photomultiplier is incapable of sustaining an anode current in excess of a few microamperes, transients damaging to the amplifier can be supported by the dynode bypass capacitors. Hence a 100K resistor is inserted in the anode line (on the PM terminal board), limiting the current to a maximum of about 1.5 mA. R1 provides a low-impedance return path for those pulses.

U2 is a monitoring stage designed to deliver ±1.25 volts, unprocessed except for the high-frequency filtering.

The peak detection is accomplished in stages U4 and U5, using $1-\mu F$ storage capacitors, C18 and C21. It is necessary in these circuits (as well as the following selector circuit) to accept the higher power drain of the LM 101 amplifier. The LM 108, unlike the LM 101, has a pair of back-to-back protective diodes across its input terminals. Excessive input current is drawn in the LM 108 whenever the input voltages are highly unbalanced, and it cannot be reduced to manageable levels without impractically high series resistors. Current into the selector circuit amplifiers, U14 and U15, must be kept small to avoid discharging the storage capacitors.

Dump pulses, to be used for dumping the peak detectors, are developed from the ROG-1 pulses by means of the U7 flip-flop and a pair of gates. To provide adequate driving signals into the FET switches (Q1 and Q2), it was necessary to provide an intermediate stage (Q3 and Q4) using both the positive and negative 10-volt supplies. Q3 and Q4 are therefore returned to -10.7 volts, and clamping circuits (C24, CR15, C25, and CR16) are then needed to produce proper DC levels for the input pulses.

The FET switches are returned to small positive bias net-
works (R28, R26, C19, R29, R34, and C22) so that the
storage capacitors (charged negatively) attempt to dis-
charge toward a potential above ground. Ground potential
is thereby achieved in a reasonable time. When the storage
capacitors reach ground level, U4 and U5 will turn on to
counteract any further rise. Thus the peak detectors are
returned to within a few millivolts of ground during the 4-
ms duration of the dump pulse.

The selector circuit is formed with a pair of unity
gain followers with the feedback closed through diodes and
having a common output (U14 and U15). The amplifier that
sees the larger input plays the role of a unity gain follower,
while the other amplifier saturates in such a direction as to
back bias its diode.

Following the selector circuit, the remaining task
prior to telemetry sampling is the logarithmic compres-
sion. A very accurate logarithmic characteristic can be
obtained over many decades by means of a transistor's
base-emitter junction. The voltage-current relationship
at this junction is given by:

$$e = 2.3 \frac{kT}{q} \log i, \tag{12}$$

where

k = Boltzmann's constant = 1.381×10^{-23} joule/°K,

T = absolute temperature in degrees Kelvin,

q = electronic charge = 1.602×10^{-19} coulomb.

At room temperature, $T \approx 300°K$, and

$$e = 2.3 \times 0.026 \log i = 0.060 \log i. \tag{13}$$

In amplifier stage U16, an input current proportional to
star pulse voltage amplitude is developed via R47 into a

virtual ground at the inverting input terminal. This current is then forced through the feedback path including one transistor of the balanced pair, Q5. The base-emitter drop at this transistor is therefore given by Eq. (13).

The second transistor of the pair, Q5, is connected as a diode with a constant current source (CR21 and R55, R56). Therefore its base-emitter drop is constant, so that any change in common emitter potential is accurately transferred to the input terminal of U19. Because of the grounded base in the first transistor of Q5, U19 is driven by a voltage that is the log of the input of U16.

To obtain an output scale of 1.5 volts per star magnitude, the gain of U19 is set accordingly. The input to U19 as given by Eq. (13) is 60 mV per decade. Since there are 2.5 star magnitudes per decade, we require an output of 3.75 volts per decade. Hence the gain of U19, as determined by R57, R62, and R67, is made equal to 3.75/0.06 = 62.5.

The output slope of 1.5 volts per star magnitude can be offset as desired by means of resistors R55 and R56. The output of U19 will be zero when the input current to U16 equals the balancing current through R55 and R56. This zero point is maintained over the temperature range by the balanced stage Q5. For true temperature stabilization, it is also necessary to correct for the slope, which changes by 0.33% per degree, as indicated by Eq. (12). The function of R57 is to supply the required gain correction. At 25°C, R57 and R62 in parallel equal 1.83K. At 55°C, R57 increases to 5.88K, making the parallel combination 1.98K. The overall gain, relative to 25°C, is 330/300 × 1.83/1.98 = 1.018. At -25°C, R57 is 3.1K, giving a parallel combination of 1.52K. The overall gain, relative to 25°C, is 250/300 × 1.83/1.52 = 1.01. Temperature testing of this log amplifier has verified its ability to hold variations down to a few percent.

The timing channel is fairly straightforward. It should be noted that it is difficult to clamp the LM 108

with an ordinary zener diode connected to the appropriate internal point (pin 9 for the flatpack). Hence, to present correct levels to the following digital circuit, an external clamp consisting of R33 and CR14 is used. R40 and R41 raise the low level slightly so that the J_1 terminal of U7 never sees a negative voltage.

The 54L95 (U13) operates in either of two modes, as determined by the level at pin 6. When high, U13 is loaded anew from the corresponding four stages of U12 at each clock pulse. As such, it keeps pace with the changing count in U12. When pin 6 goes low because of an ROG-2 pulse, U13 becomes a shift register with a serial output available at pin 9. The next four clock pulses will deliver a four-bit count. The correct count is represented by the level at pin 9 when the clock goes high (the actual shifting occurs when the clock goes low). It is essential for the leading edge of ROG-2 to occur slightly later then the negative edge of the clock pulse. To guarantee this essential timing, the delay circuit, R71 and C36, was inserted into the ROG-2 line.

Power considerations dictate the choice of polarity for the comparator U18. The output clamp circuit, R66, and CR23, consumes more power in the low condition. It is therefore desirable for the low state to correspond to the presence of sun, a condition that will exist a small portion of the time. A two-transistor switch, Q100 and Q101, controls the 10.7-volt line to the photomultiplier power supply. R51 has been set at 16.2K so as to cause tripping at about 185-μA input current (the current delivered by two sun sensors in parallel at 53° from the sun). A small hysteresis is introduced into the U18's switching characteristic through the positive feedback resistor R64 so as to avoid chattering in a marginal condition.

TEST AND CALIBRATION

The star sensor was tested both in the laboratory and in the field. In the laboratory, the unit was calibrated

- 48 -

using simulated stars. The instrument was then tested using the night sky.

The SAS-B star sensor telemeters data that can be classified in two categories: aspect data and engineering housekeeping data. The aspect data consist of the amplitude of the detected star pulse and the time (± 3 ms) at which it occurred. Engineering housekeeping data consist of sensor temperature, unprocessed analog output of the sensor, high-voltage on/off telltale, and low-voltage on/off telltale.

Laboratory Test Results

The photometric testing of the star sensor was conducted in a calibrated light tunnel using a calibrated tungsten filament source. This luminous radiation passes through a series of neutral density filters, a light chopper, and a small aperture to simulate a point source of calibrated starlight. The chopper is operated at the speed that simulates the star signal pulse duration time for a satellite spinning at 1/12 or 1 rpm. The star sensor is placed in the light tunnel at a predetermined location to yield a specific star visual magnitude from +1 to +4. Since the star does not appear at infinity for this test, it is necessary to make the proper lens focus adjustment by means of a precalculated thickness spacer between the sensor optic and the "N" slit reticle. It is essential that the entire star image fall within the confines of the "N" slit opening.

This test was performed with all the electronics operational. The star sensor output was fed into a suitcase field tester which contained a duplicate of the satellite signals. The test yielded several calibration points that were later compared with further test results at NASA, Goddard Space Flight Center. The two tests indicated star amplitude correlation to within 0.3 of a star visual magnitude. These tests were performed at both the 1/12 and 1 rpm spin rates. The star amplitude calibration data are given in Fig. 21.
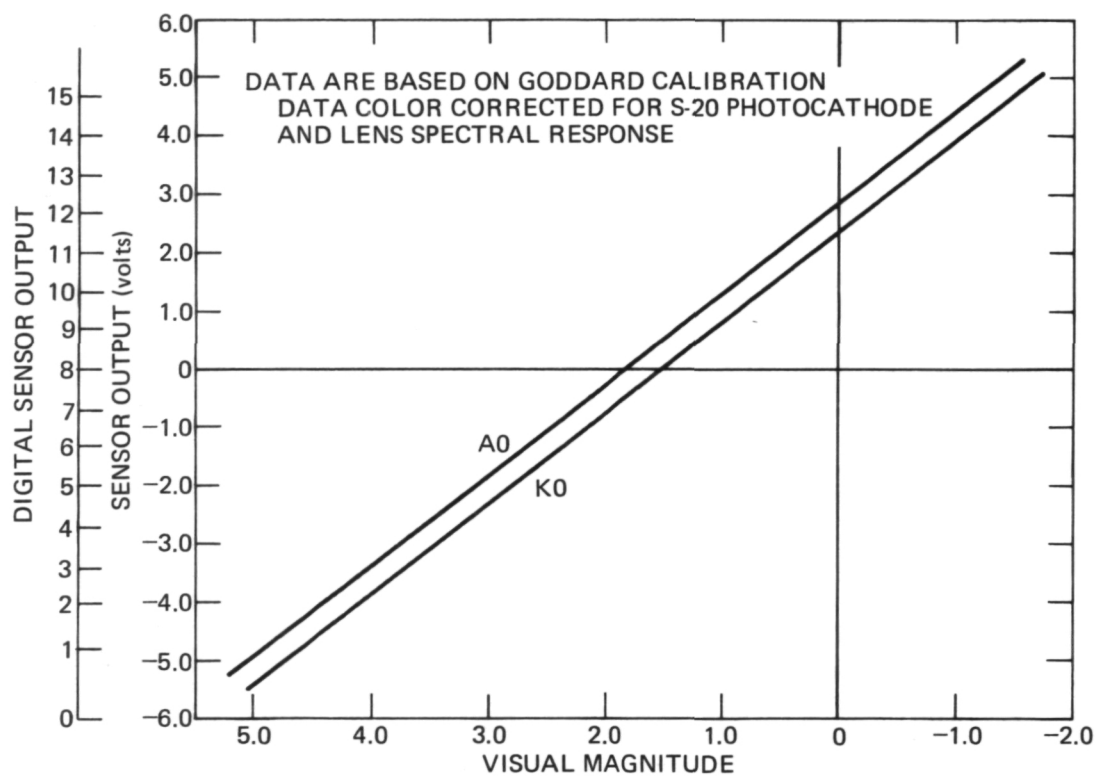
Fig. 21 STAR SENSOR OUTPUT VERSUS STAR MAGNITUDE (LABORATORY MEASUREMENTS)

Amplitude data are shown both in terms of the sensor's analog output and the discrete digital levels produced by the satellite's A/D converter. The data are good for stars transiting the sensor at 0° elevation relative to the optic axis. As the elevation angle changes, there is a slight variation in the output (Fig. 22). The data given in Fig. 21 are based upon measurements made at NASA/GSFC correlated to field test data. The curves should be accepted as accurate to ±0.1 of a visual magnitude.

The data in the telemetry stream represent stars crossing the three slits of the "N" shaped reticle. The first and third pulses establish within ±1 arc minute the azimuthal position, at particular times, of the sensor's optic axis. Their relation to the second pulse determines the elevation of the optic axis relative to the particular star observed. To determine these positions, the exact location of each slit with respect to the optic axis must be known. Figures 23 through 25 show the location of each slit relative to the optic axis as a function of the elevation angle. The curves are least square fits to laboratory mapping data averaging the azimuthal position of the slit edges at each elevation angle.

Once the position of the star is known relative to the optic axis, the position must then be transferred to the experiment's coordinate system.

To verify the proper operation of the sensor's timing channel, a lens cap was fitted with light-emitting diodes. These diodes were driven by 8-ms pulses to simulate star signals in the fast mode. The 8-ms driving pulses were, in turn, developed from the gate pulse with an adjustable delay. As the delay was varied, the four-bit count delivered by the timing channel was observed. This test confirmed that the four-bit count did in fact indicate elapsed time (in 3-ms increments) between the star pulse and the readout gate.
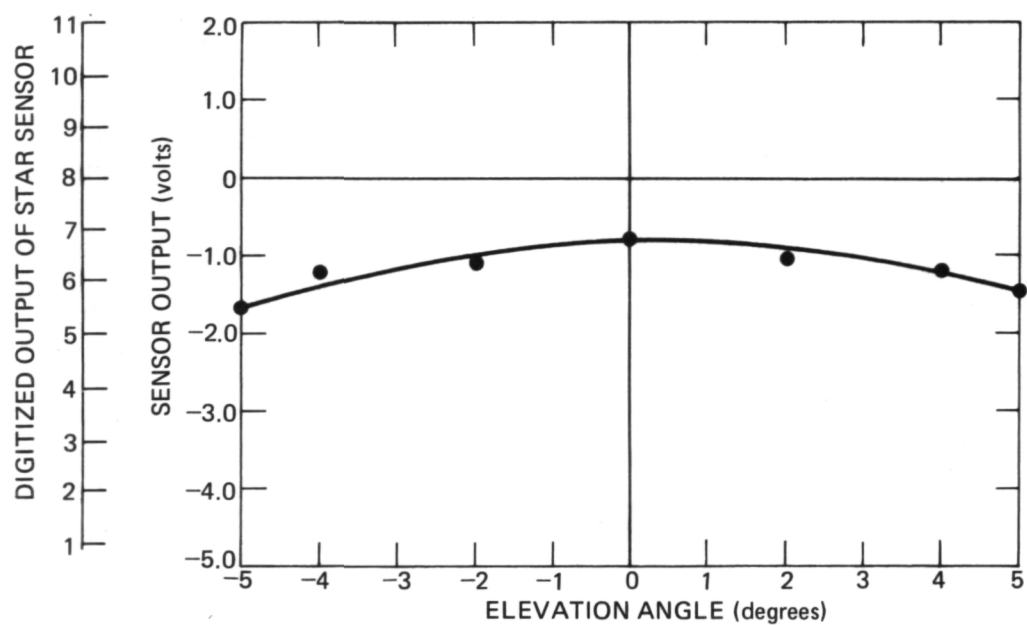
Fig. 22   VARIATION IN STAR SENSOR SENSITIVITY VERSUS ELEVATION ANGLE
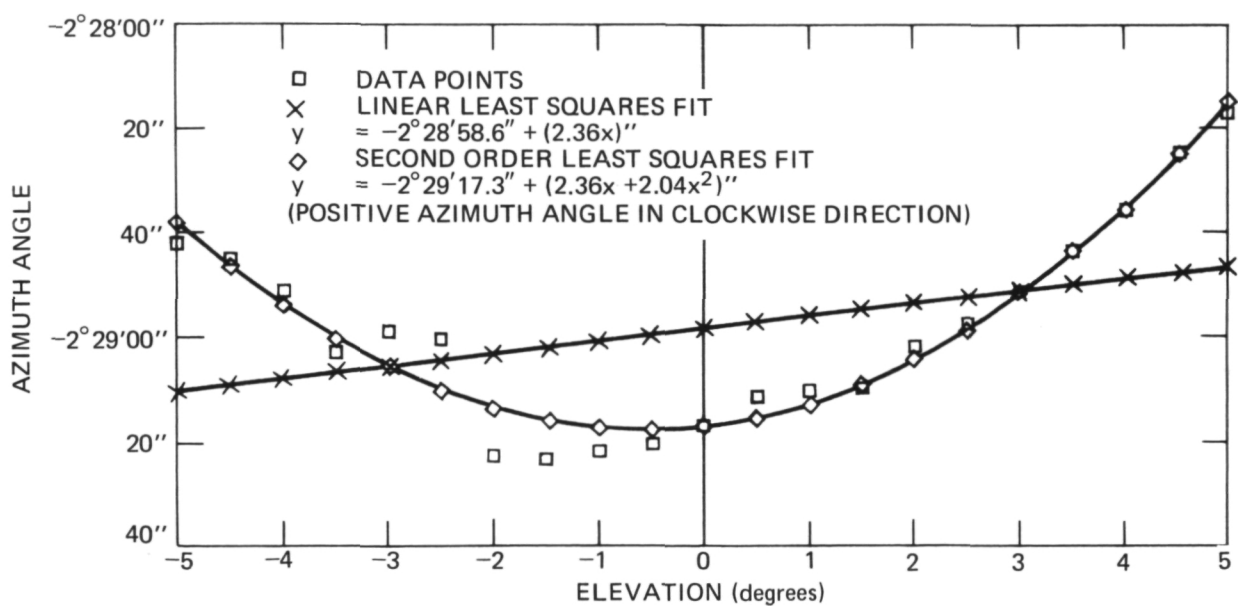
Fig. 23 RETICLE MAPPING SLIT NO. 1
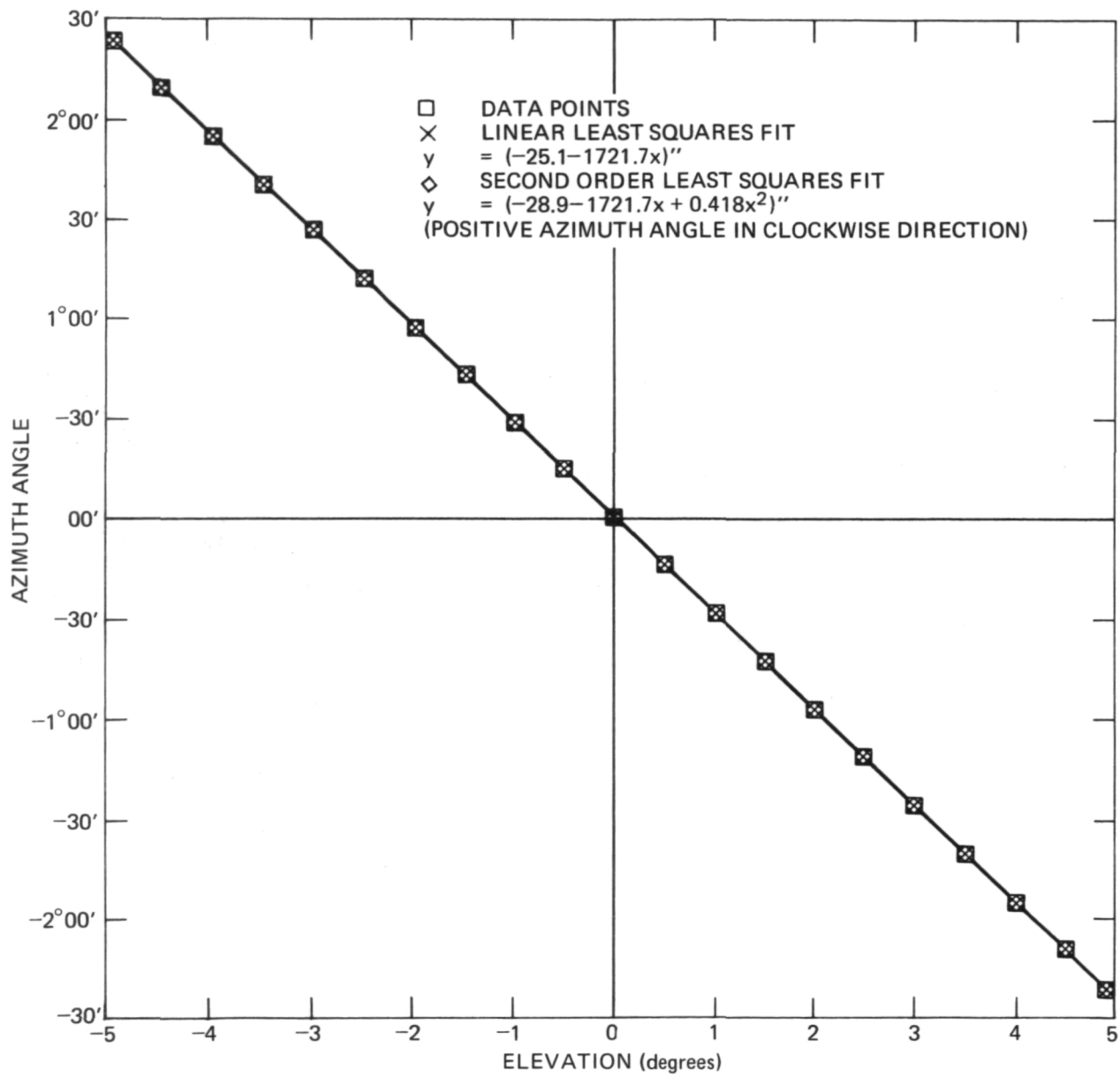
Fig. 24   RETICLE MAPPING SLIT NO. 2
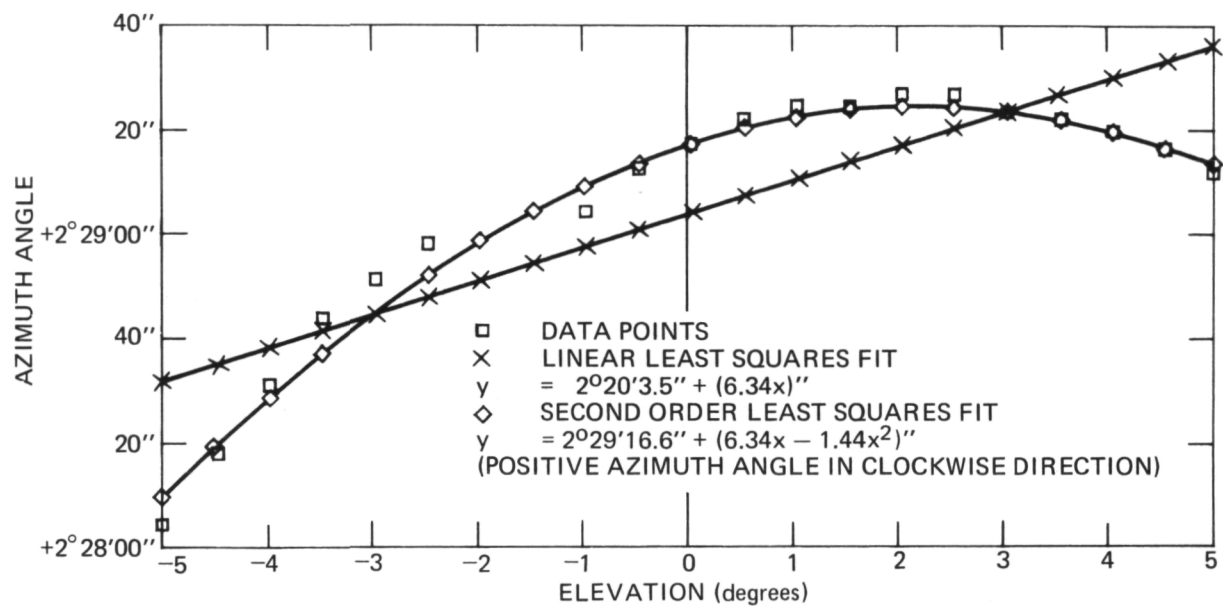
Fig. 25   RETICLE MAPPING SLIT NO. 3

Field Test Results

The star sensor was calibrated in the laboratory at APL using a standard 2870°K source and then checked at NASA/GSFC, with good correlation. Field tests were conducted at the High Altitude Observatory, Climax, Colorado. The sensor was mounted on a motor-driven assembly to simulate scanning speeds of 1/12 and 1 rpm. A portion of the sky was swept out (from Arcturus to Polaris), and the readouts were recorded on tape. Gain and threshold settings were based on these tests.

Using the response to the star Arcturus (a K type), and knowing the slope of the logarithmic amplifier, an output calibration curve was drawn (Fig. 26).

With a stationary sensor aimed in the vicinity of the star Vega, an rms noise of about 8.25 mV was observed in the fast mode at the linear amplifier output. For this gain, the output of a +4 visual magnitude K0 star is 47 mV. Thus the experimentally observed signal-to-noise ratio (in the absence of signal) is 47/8.25 = 5.7 = 15.1 dB. This is 70% of the calculated value.

A significant portion of this higher observed noise is attributed to the atmosphere. At the 11 000-foot altitude where these tests were performed, two-thirds of the Earth's atmosphere was still above the sensor.

There is a remarkably close correlation between the laboratory calibration shown in Fig. 21 and the field data shown in Fig. 26.
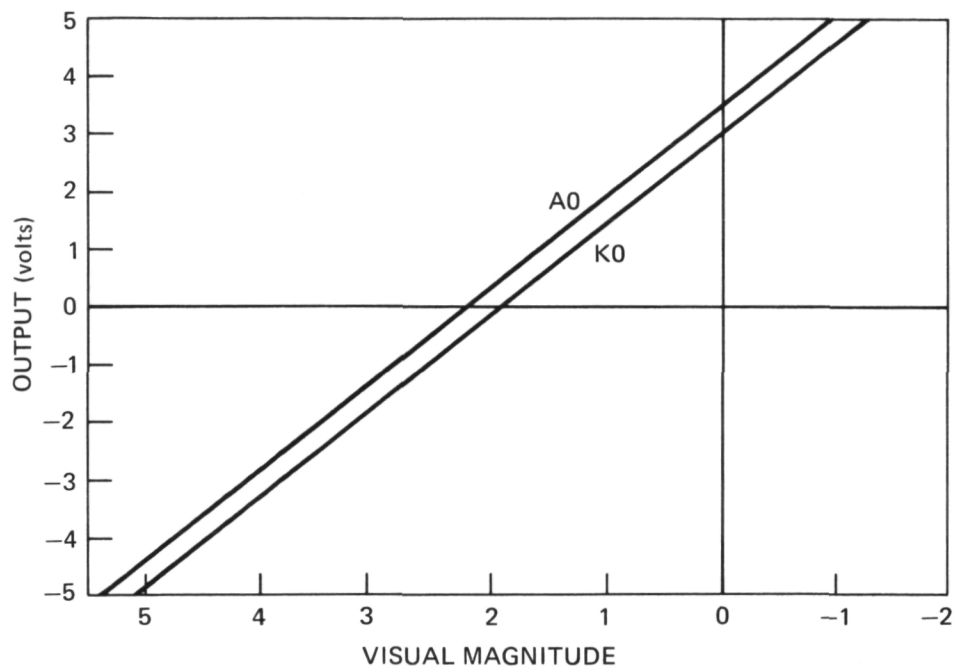
Fig. 26   STAR SENSOR OUTPUT VERSUS STAR MAGNITUDE (FIELD MEASUREMENTS)

Page intentionally left blank

3. LIGHT SHADE

DISCUSSION

Since the star sensor must detect stars of +4 visual magnitude within 60° of the sun line, a highly sophisticated light shade that will provide an attenuation of 10^{10} is needed. A background attenuation of approximately 10^3 is obtained in the associated star sensor. The satellite is in a circular, near-equatorial orbit at an altitude of 550 km. The satellite orientation is arbitrary, and therefore the light shade must also provide high attenuation against Earth shine with somewhat lesser demand on lunar illumination.

Boundary limits on the light shade length and diameter prior to satellite launch are imposed by the payload envelope within the booster fairing or heat shield. The light shade is to be no more than 3 inches long by 7 inches in diameter. It is designated to work with a 2-inch aperture, f/2 Super Baltar Bausch & Lomb lens. It is obvious, without detailed computation, that the length of the light shade must be considerably greater than the lens diameter. This without question necessitates a design for a light shade that can be compressed during the satellite launch phase and extended subsequent to booster separation. By necessity, the light shade must be lightweight because of critical booster-payload matching for a 550-km Scout rocket launch. The deployment mechanism for the light shade must be simple and reliable and should consume very little, if any, power. Armed with this set of boundary conditions, a design effort was initiated.

DESIGN INVESTIGATION

It was readily determined at the onset of this effort that a two-stage light baffle would be required. Figure 27 shows the basic design concept. It is imperative that the first stage of the baffle be in no way visible to the star
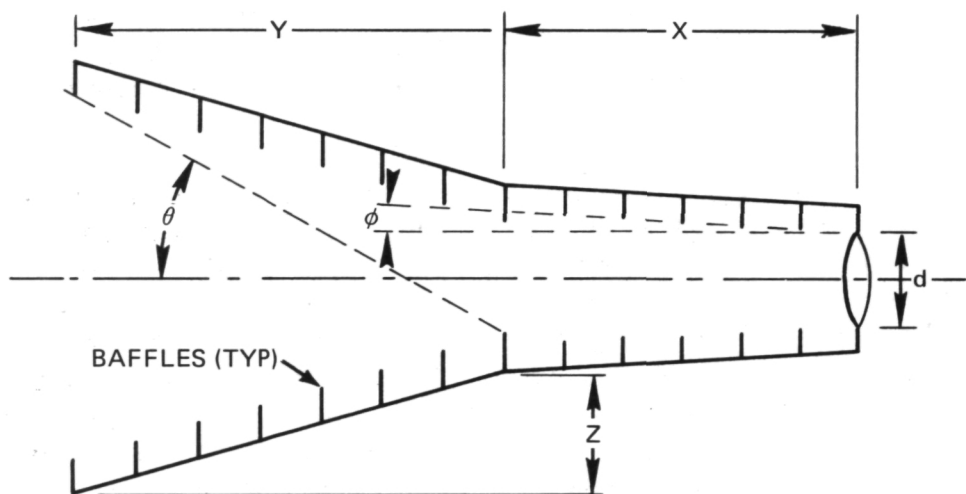
Fig. 27   LIGHT SHADE BASIC GEOMETRY

sensor optic. The second stage tends to function as an absorber of scattered light emanating from the first stage because of off-axis illumination. It is essential that the design give optimum performance for minimum light shade dimensions. With the aid of Fig. 27, the following equations were developed:

$$\frac{Y}{Z} = \frac{X}{d + X \tan \varphi} \ . \tag{14}$$

$$\tan \theta = \frac{d + 2X \tan \varphi + Z}{Y} \ . \tag{15}$$

Combining Eqs. (14) and (15) and solving for Y:

$$Y = \frac{Xd + 2X^2 \tan \varphi}{X \tan \theta - d - X \tan \varphi} \ . \tag{16}$$

The length, L, of the illumination shade is X + Y:

$$L = X + Y = \frac{Xd + 2X^2 \tan \varphi}{X \tan \theta - d - X \tan \varphi} + X \ . \tag{17}$$

Differentiating L with respect to X, setting the result equal to zero, and solving for X will yield the minimum value of L that may be used in the design.

$$\frac{dL}{dX} = \frac{X^2 \tan^2 \theta - X^2 \tan^2 \varphi - 2Xd (\tan \varphi + \tan \theta)}{[X (\tan \theta - \tan \varphi) - d]^2} \ . \tag{18}$$

$$\frac{dL}{dX} = 0.$$

$$X = \frac{2d}{[\tan \theta - \tan \varphi]} \quad (\text{for } L_{min}). \tag{19}$$

Substituting this value of X back into Eq. (17) yields:

$$L_{min} = \frac{2d\,[\tan\theta + 3\tan\varphi]}{[\tan\theta - 2\tan\varphi]\,[\tan\theta - \tan\varphi]}$$

$$+ \frac{2d}{[\tan\theta - \tan\varphi]}\,. \qquad\qquad (20)$$

The following options were among those considered in the selection of a light shade design.

Option I

Figure 28 is a schematic of this light shade design. The first stage consists of a conical section attached to a cylindrical section. The interior of this stage is highly reflective to repel the major portion of the incident illumination. The objective optic sees no portion of this stage. The second stage consists of a truncated conical section outfitted with a series of baffles. This entire section is treated with a very dull black, optically absorbent paint. The edges of the baffle rings are razor sharp to keep light scattering effects to a minimum. It is mechanically conceivable that this design could be folded or compressed into a very-low-profile cylinder. The folding of the first stage would require a much more complex mechanism. The external surface of the light shade is thermally treated for operation in a space vacuum solar environment.

Option II

This design (Fig. 29) is similar in concept to the Option I design with the exception of the first stage, which is an absorbent wide-angle cone. A variance of this design has been built using a reflective conical first stage. The gross test results of the reflective and the absorbent first stages are very similar, indicating that most of the high-level illumination is attenuated by the second stage. The model shown was built merely for rudimentry laboratory testing to establish some general design criteria.
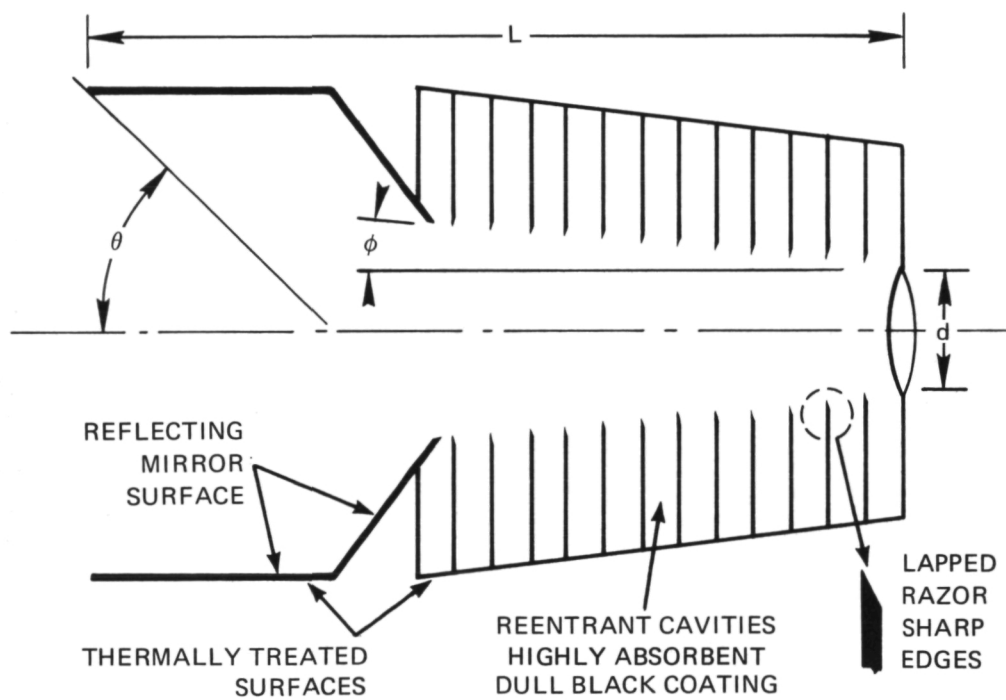
Fig. 28   OPTION I LIGHT SHADE
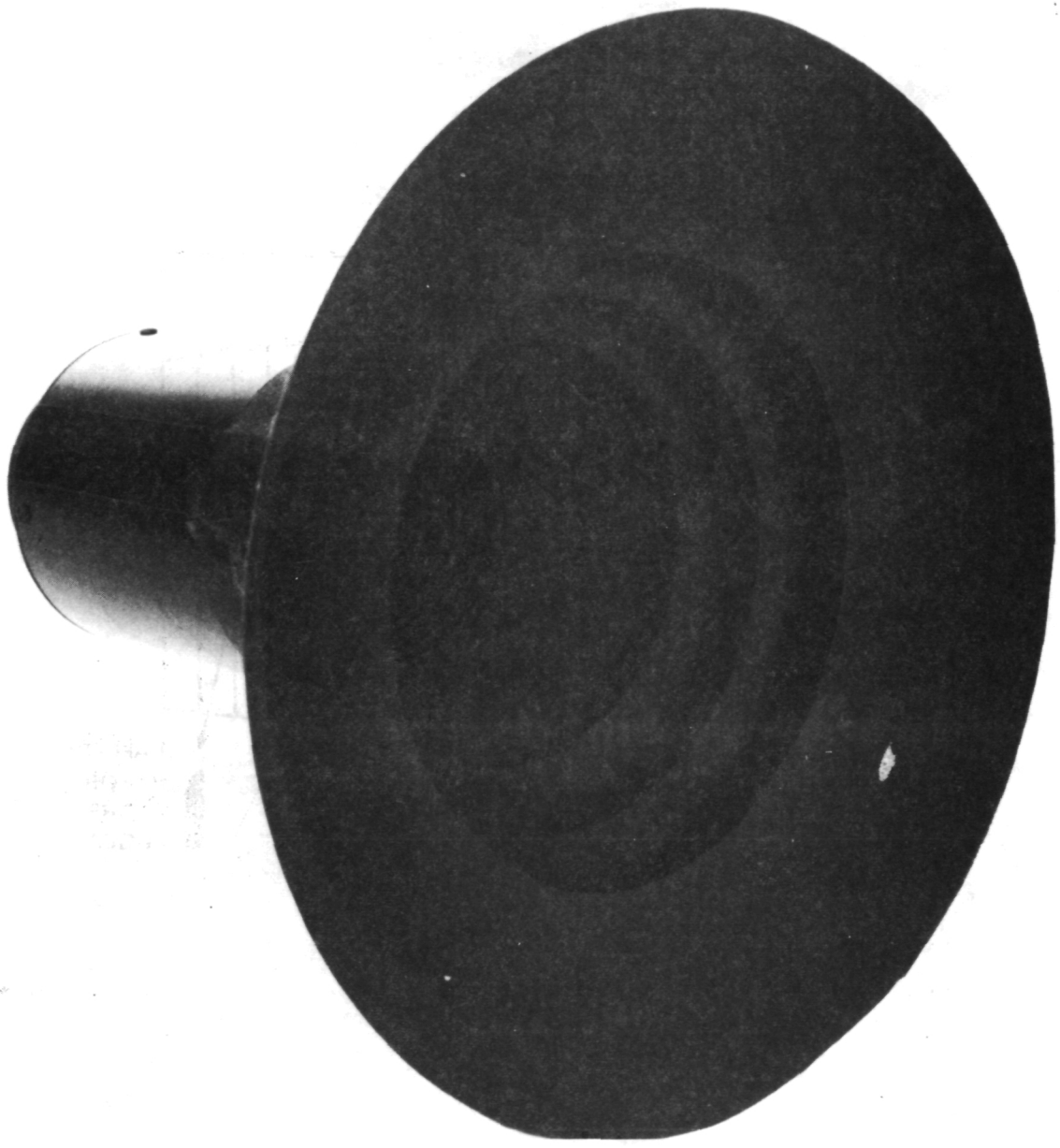
Fig. 29   OPTION II LIGHT SHADE

Option III

This design (Fig. 30) is considerably more complex. The first stage consists of a complex reflective cone that is segmented to include absorbent doughnut-shaped reentrant cavities. It is intended for the mirror-like reflective conical segments to reject almost all the incident illumination. The small portion of the illumination that is scattered from the razor sharp edges in a sphere of 2π steradians is partially reflected and partially absorbed by the reentrant cavities. The portion of the scattered illumination that is heading downward into the system toward the objective optic is again introduced to the absorbent medium of the second stage. The second stage is similar in concept to the previously discussed designs. From a mechanical viewpoint, this design presents an intriguing compression problem. Although it is photometrically promising, a good folding design is difficult to formulate.

Option IV

A two-stage, fully baffled design is illustrated schematically in Fig. 31. The first stage is a continuation of the second stage with the exception of the basic cone half-angle. No portion of the first stage is viewed by the objective optic. The second stage is divided into two portions, one portion being inside the satellite skin and the other external to the satellite. All internal sections of the light shade are coated with a dull 3M optical black velvet paint. All edges are razor sharp to minimize light-scattering effects. Mechanically, this design is the most plausible for prelaunch compression.

DESIGN SELECTION

Predicated upon mechanical simplicity and good photometric properties, Option IV was selected. This design offered good promise for baffle compressibility. Its good photometric properties were proved in an initial test mockup model.
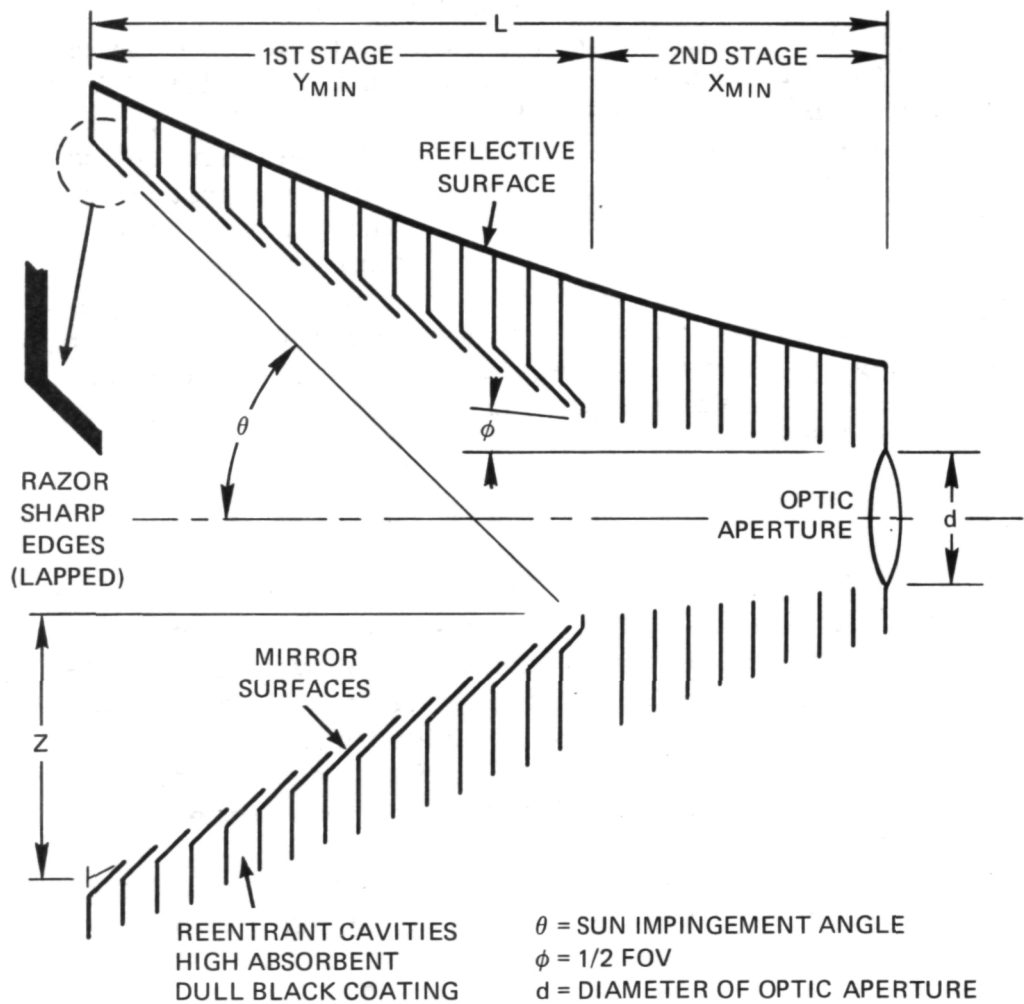
Fig. 30   OPTION III LIGHT SHADE

SHARP EDGE TO SUN   (TYP)

ϕ

θ

CONTINUOUS BOND
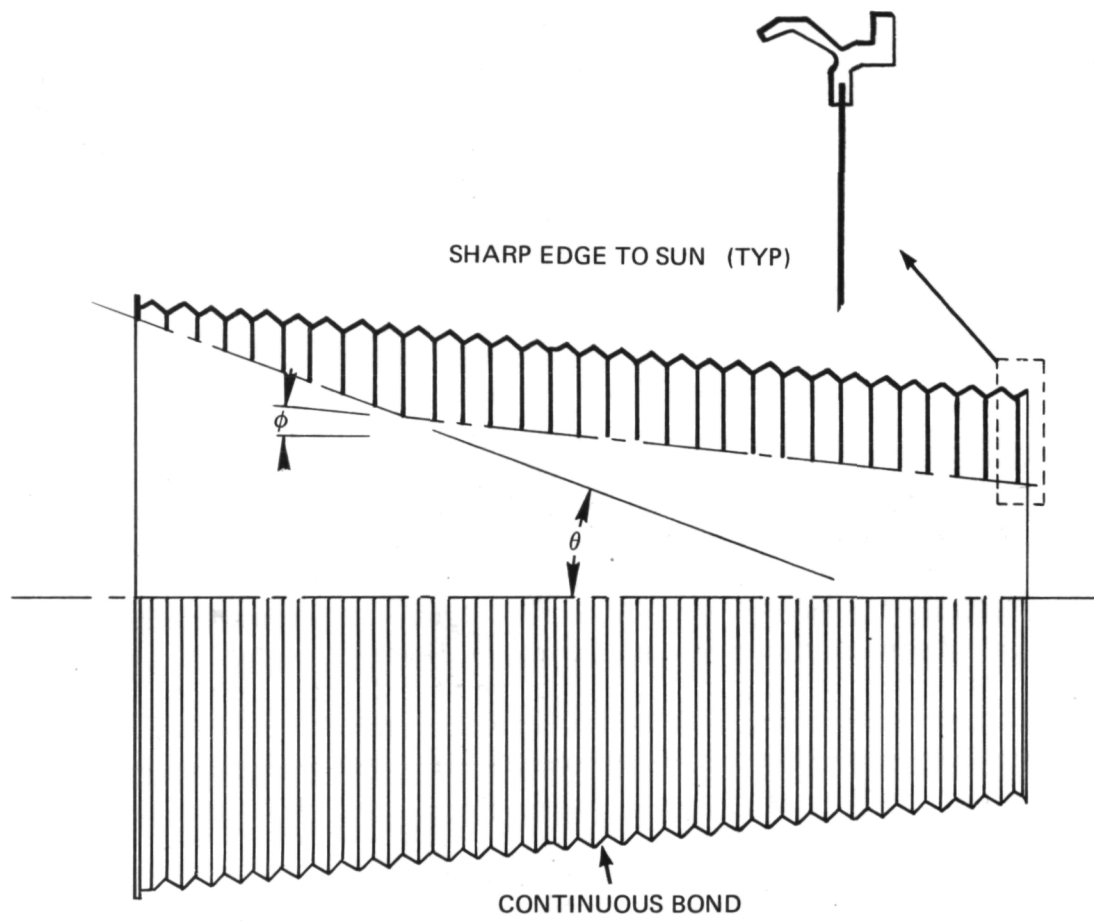
Fig. 31   OPTION IV LIGHT SHADE

The final design evolved in the form of a compressible rubber boot made of RTV 630 Silastic. The boot forms a carrier vehicle for the many ring baffles inserted and glued in place with RTV 630. The boot plus baffles can be compressed in an accordian-type fold. Figure 31 shows the design form. The basic Silastic boot material is black, which is good for the light shade interior. The exterior of the boot is a highly reflective white that is obtained by impregnating the Silastic material with zinc oxide power combined in paste form with RTV 630 Silastic rubber.

The light baffles are made of thin (0.012-inch-thick) aluminum. The surface has a black anodized finish followed by a coat of 3M dull black velvet paint. This paint is very carefully sprayed on to avoid buildup on the razor sharp edges. The entire assembly is housed in a two-part aluminum container. One portion of this container is fastened to the satellite shell, and the other portion is fastened to the large end entrance port of the light shade. In the compressed, or prelaunch, mode the light shade is confined within this two-piece housing. Figure 32 shows the light shade in its compressed form. A lever-type latching mechanism has been designed to lock the light shade in its compressed form. When this locking mechanism is released, the light shade automatically pops open like a jack-in-the-box. The Silastic boot provides the necessary spring action to cause deployment of the light shade. The release mechanism for this spring action is provided by the release of a satellite solar blade into its fixed working position. Figure 33 shows the deployed light shade. The light shade is equipped with an illumination sensor for protection of the primary sensing instrument when it is exposed to high illumination levels from the sun, earth, or other source.

The basic limitations imposed upon the light shade by use of the design Eqs. (16), (17), (19), and (20) for a 2-inch-diameter objective optic, a solar impingement angle (θ) of 45°, and a basic sensor field of view of 12° diameter require that the minimum length of the light shade be 8.35 inches. The design shown in Fig. 33 has a total length of 11.43 inches, including the portion of the second stage that
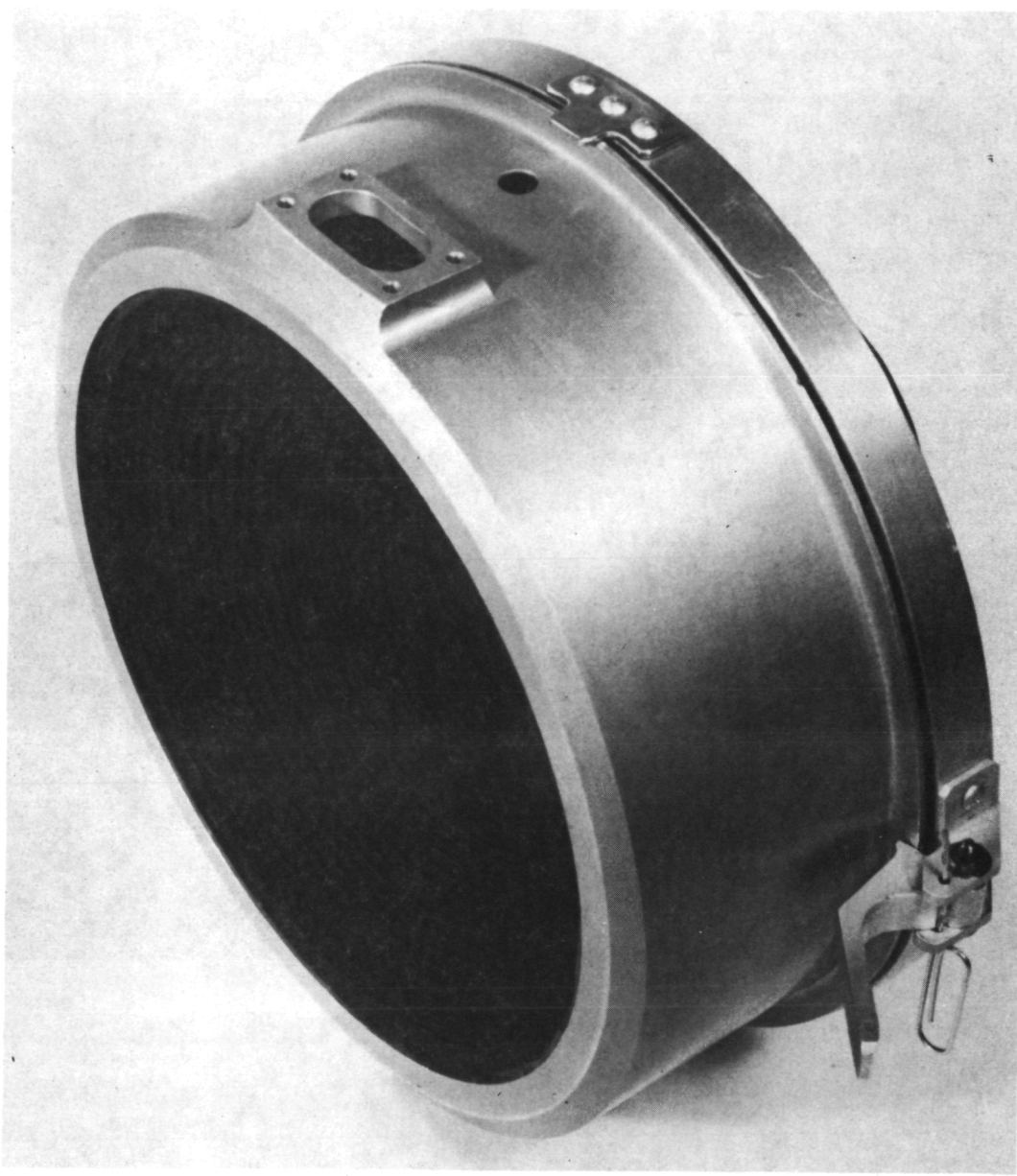
Fig. 32   COMPRESSED FLIGHT TYPE LIGHT SHADE
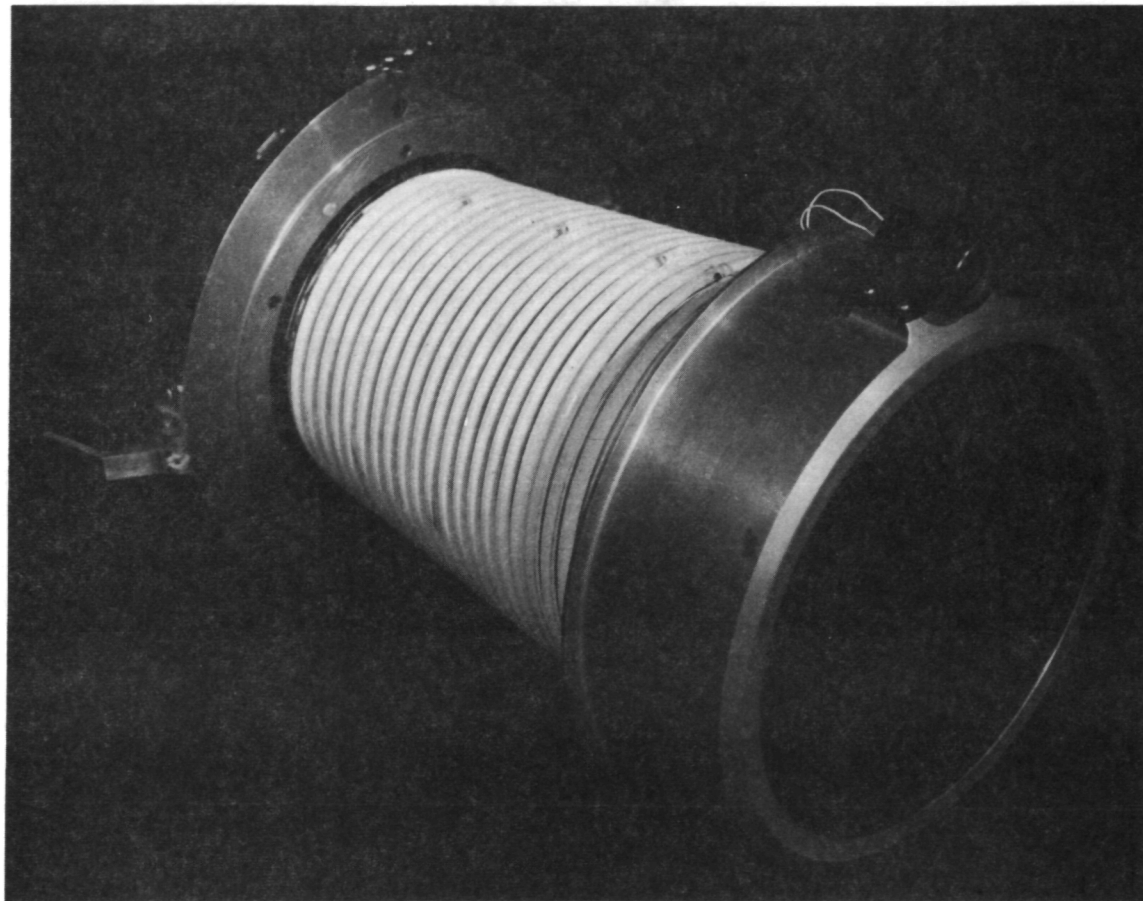
Fig. 33   EXTENDED FLIGHT TYPE LIGHT SHADE

fits inside the satellite skin. It may be noted from Figs. 30 and 32 that the light shade is equipped with a flexible boot that forms a light-tight seal with the objective optic of the associated instrument. The selected design has the transfer characteristic shown in Fig. 33. Attenuation of better than 10^6 is obtained at 45° in laboratory measurements. Laboratory measurements beyond this level are very difficult and extremely expensive. To improve measurement accuracy for the next few orders of magnitude, a very large vacuum chamber with highly sophisticated light absorption chambers is required. One of the big problems in making measurements of this type is to completely absorb light rays scattered from the light shade into the surrounding medium and back on axis into the light shade. The space environment will provide the required conditions. Figure 34 shows the anticipated space operational characteristic extrapolated from laboratory data.

All testing and measurements on the light shades were performed in a 12-foot-long light tunnel equipped with a calibrated tungsten source, a calibrated neutral density filter bank, and a high-gain photomultiplier tube sensor. The interior of the light tunnel is baffled to reduce stray reflections. Figure 35 illustrates the basic test arrangements for measuring the light shade transfer characteristic. The sensor used to make these measurements was a 2-inch-diameter photomultiplier to simulate the aperture of the 2-inch-diameter objective optic of the star sensor. The full entrance aperture of the light shade was illuminated for all angles of test.

Deployment of the light shade was tested numerous times after 2 to 3 weeks of compression. The shade always returned to its natural stress-relieved position. In addition, thermal vacuum outgassing tests were performed on the RTV 630 Silastic rubber boot. There was no evidence of outgassing after a week of thermal vacuum cycling from -20° to +120°F.
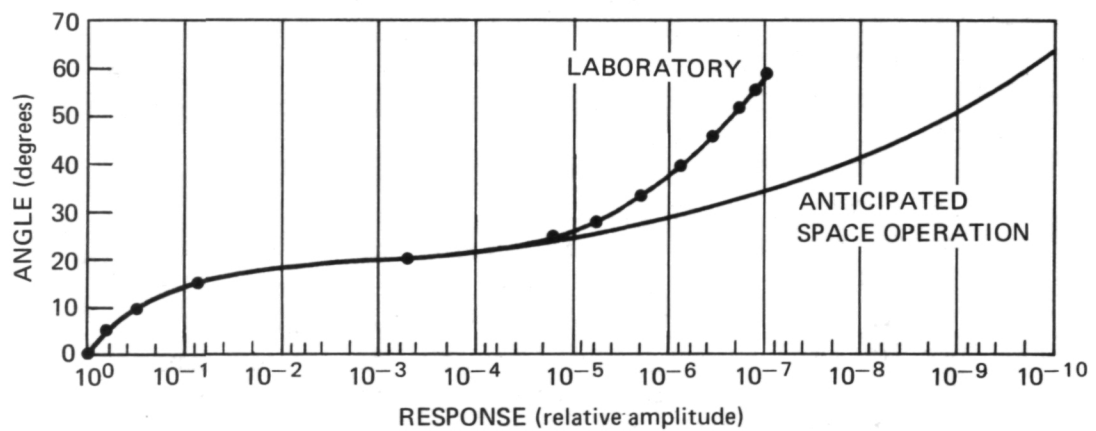
Fig. 34   LIGHT SHADE TRANSFER CHARACTERISTICS
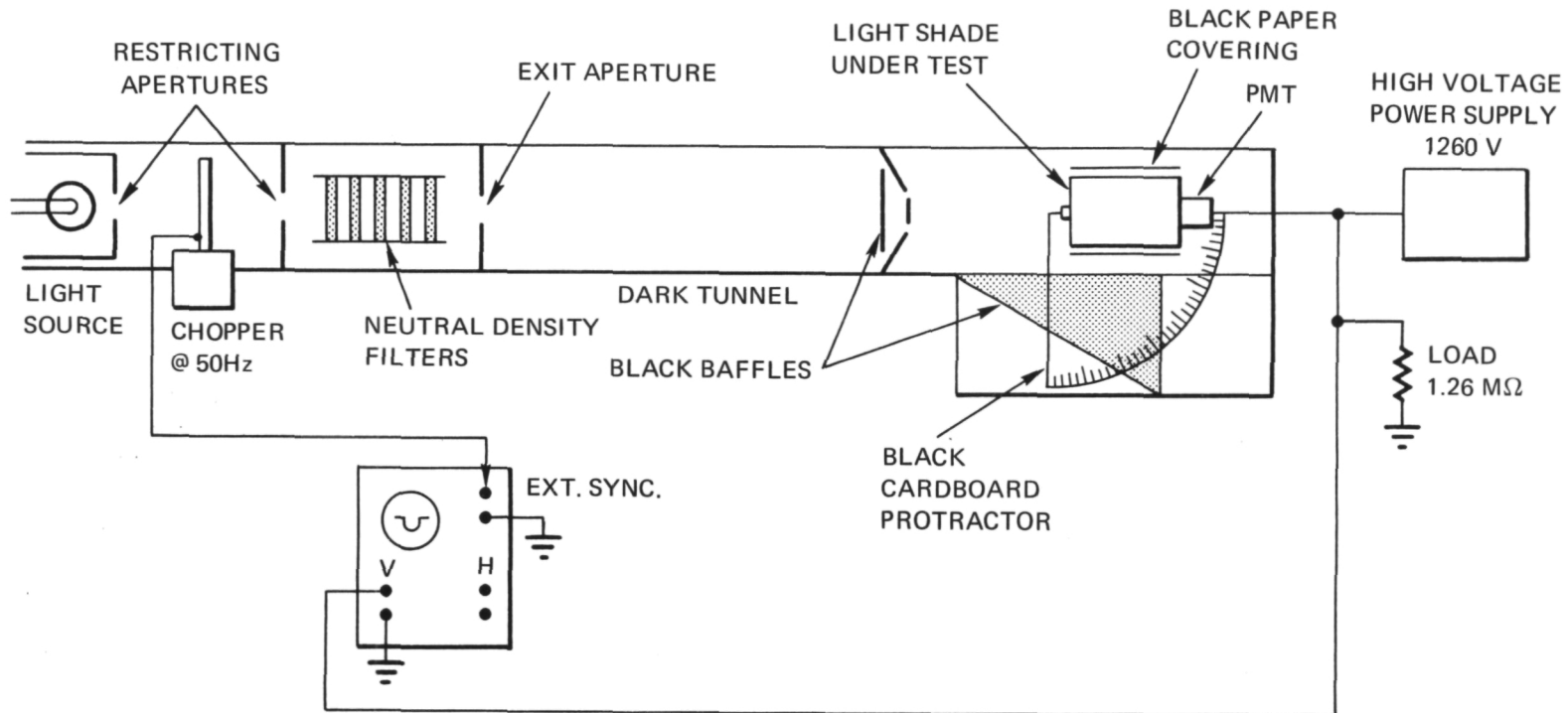
Fig. 35 LIGHT SHADE TEST ARRANGEMENT

Page intentionally left blank

4. ILLUMINATION SENSOR

An illumination sensor was used in conjunction with a star sensor/mapper to detect overload irradiance conditions that would result in damage to the primary instrument, i.e., the star sensor. For the case of the SAS-B mission, in which a 550-km orbit is to be achieved, solar, lunar, and earth irradiance on the satellite star sensor should be examined.

OPTICS

The general design layout of the illumination sensor is illustrated in Fig. 9. It may be noted that the sensor units have a high-purity quartz cover plate, whose purpose is to offer radiation protection. Although this is not an important feature for the SAS mission, it has been most significant on other missions. The use of parallel plate refractors on either side of a lens has the effect of shifting the focal plane or the effective field of view and must be taken into account in the sensor package design. When the refractor plate is placed in front of the lens, the effective field of view of the system is affected. When the refractor plate is placed behind the lens, a shift in the focal plane occurs. While no significant deviation in ray path occurs for near-paraxial rays, off-axis rays are subjected to considerable displacement. The path deviations encountered (Fig. 36) may be expressed as follows:

$$d = t \sin \varphi \left(1 - \frac{n}{n'} \frac{\cos \varphi}{\cos \varphi'} \right). \qquad (21)$$

The angle of refraction may be calculated from Snell's Law:

$$n \sin \varphi = n' \sin \varphi', \qquad (22)$$
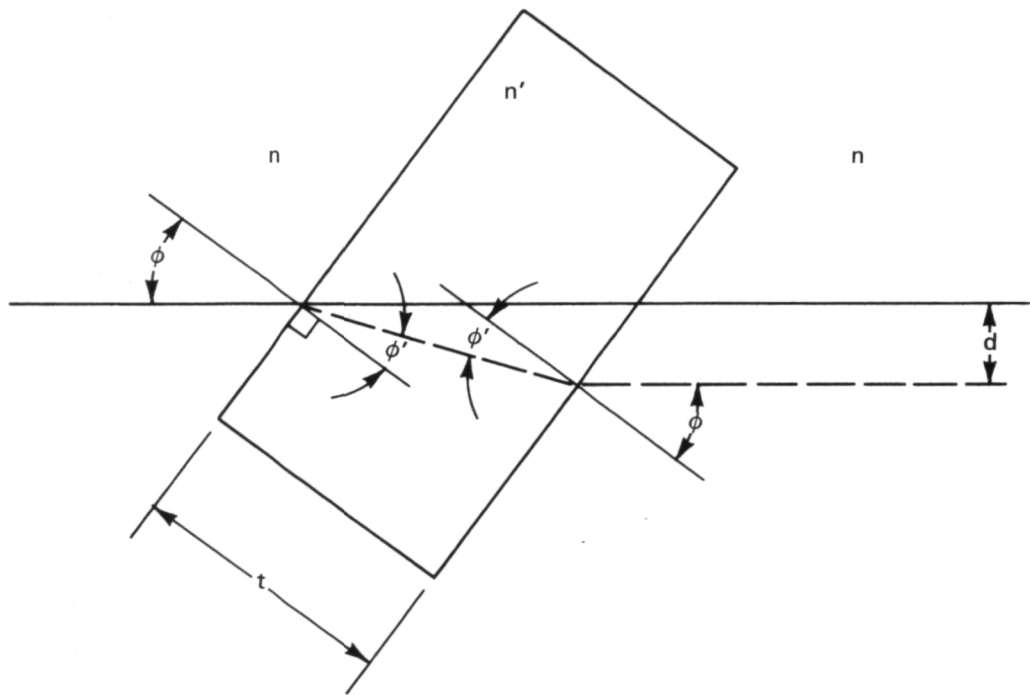
Fig. 36 PARALLEL PLATE REFRACTOR

where n and n′ are the refractive indexes of air and quartz, respectively. For the case at hand in which a refractor plate 0.2 inch thick is placed in front of the lens, a ray with φ = 30° will result in a path deviation of 0.0394 inch. The effect of this path deviation appears as an effective change in the angular field of view.

Placement of a refractor plate, such as the heat filter (Fig. 9), between the lens and the image plane would cause a similar path deviation of a skew ray at an angle, α. More significant would be a change, δ, in the effective back focal length of the lens (Fig. 37). The thickness of the heat filter (Bausch & Lomb 90-21) is 0.080 inch. The shift in back focal plane is given by:

$$\delta = \frac{d}{\sin \alpha} \cdot$$ (23)

The path deviation caused by the heat filter is 0.0278 inch for a 30° off-axis ray. The corresponding deviation in the focal plane is 0.0139 inch.

It is desired that the illumination sensor exhibit a sharp cutoff characteristic; therefore a lens has been incorporated into the design. This is a 7-mm focal length, 5-mm diameter objective with an effective speed of f/1.75. The detector, a 1-cm^2 silicon solar cell, is masked to present a sensitive area 0.274 inch in diameter for a 53° field of view. The location of the detector takes into account the discussed focal plane shift.

PHOTOMETRY

The illumination sensor transfer characteristic is shown in Fig. 38. The response to the earth, the sun, and the moon will be examined.
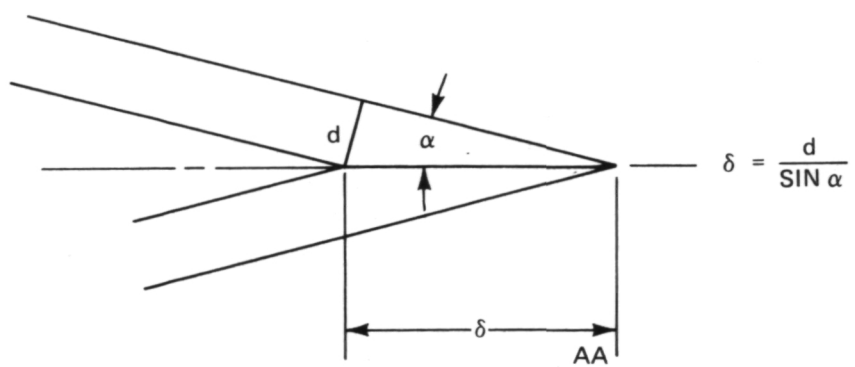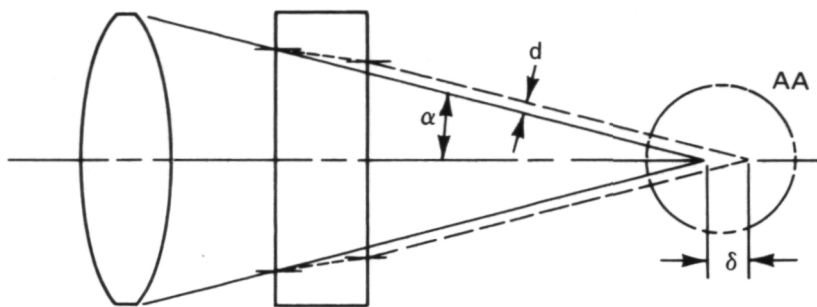
Fig. 37   EFFECTS OF PARALLEL PLATE REFRACTOR
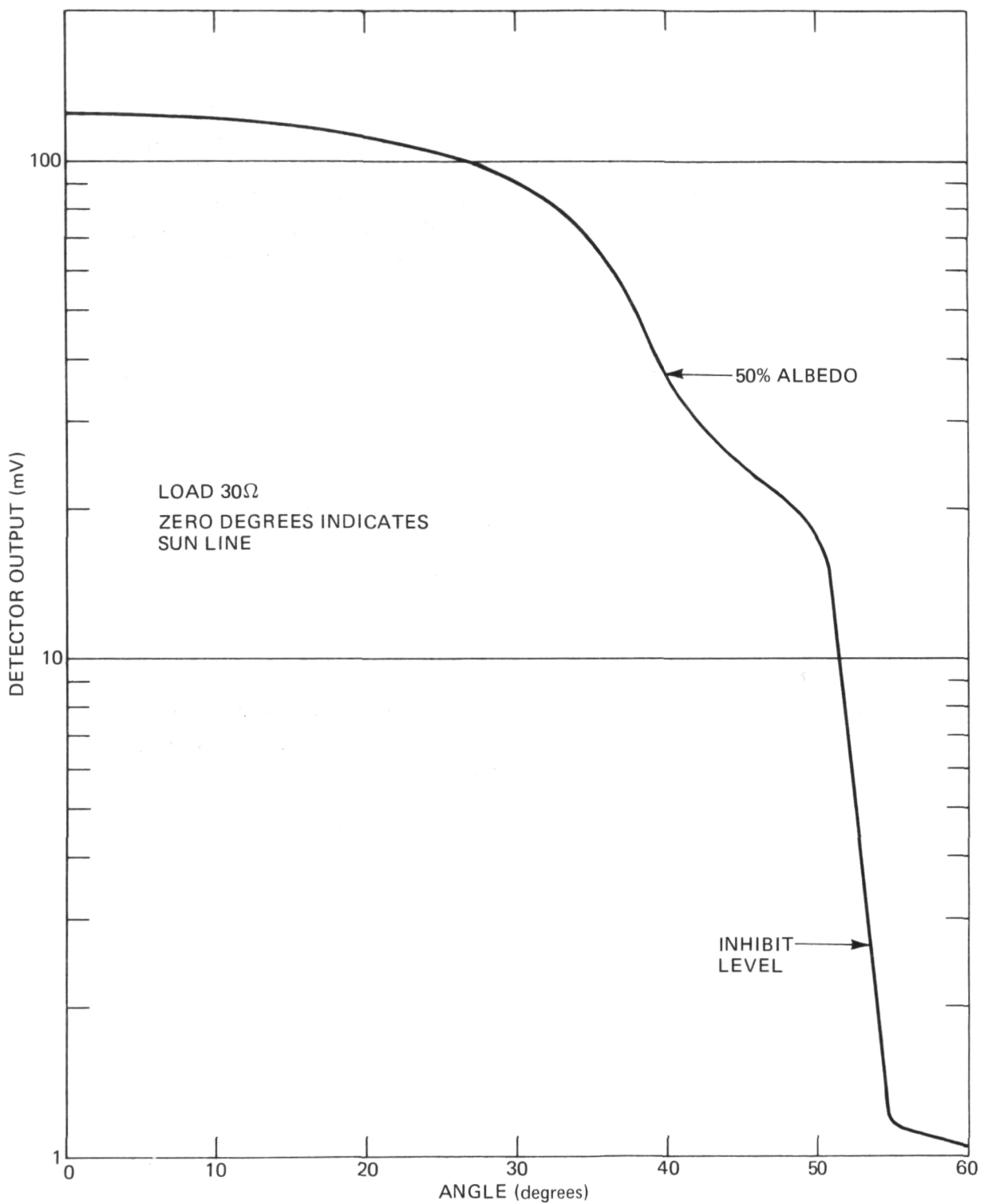
Fig. 38   ILLUMINATION SENSOR TRANSFER CHARACTERISTIC

Earth

The earth subtends 134° from a satellite altitude of 500 km. The image of the earth's disk will therefore cover the entire sensitive area of the detector. The earth's brightness, if taken as 10^4 footlamberts (fL) will yield an input to the detector of 3.45×10^2 footcandles (fc) for 50% albedo and a filter-transmission/optical-loss factor of 0.85.

$$E = \frac{B}{4(f/\#)^2} . \tag{24}$$

where

B = brightness in footlamberts,

E = illumination in footcandles,

$f/\#$ = optic speed.

The sensitivity of the silicon solar cell for a 30-ohm load is given as 5.4×10^{-3} ampere/lumen. The luminous flux incident on the detector is computed as follows:

$$\begin{aligned} \text{Lumens} &= \text{footcandles} \times \text{detector irradiated} \\ &\quad \text{area (ft}^2) \\ &= (3.45)\, 10^2 \times 4.09 \times 10^{-4}\ \text{ft}^2 = \\ &\quad 0.141\ \text{lumen.} \end{aligned} \tag{25}$$

The detector output current, I_E, resulting from earth shine is:

$$\begin{aligned} I_E &= \text{sensitivity} \times \text{lumens} \\ &= 703 \times 10^{-6}\ \text{ampere.} \end{aligned} \tag{26}$$

For the star-sensor/earth-shine minimum angle of approach, the reader is referred to Appendix D.

Sun

The sun has an angular subtense of 0.5° which results in a small point-like image 2×10^{-3} inch in diameter on the silicon detector. For a solar brightness of 5×10^{8} fL, one gets an illumination of 3.4×10^{7} fc with an optic efficiency of 0.85. This results in a luminous flux of 0.743 lumen on the detector. The detector output current, I_s, for the sun will then be 3.7×10^{-3} ampere.

Moon

The angular subtense of the moon, like the sun, is 0.5°. The illumination provided by a full moon on the earth's surface is given as 3×10^{-2} fc. For an optic diameter of 4 mm (0.160 inch), this yields a luminous flux of 4.185×10^{-6} lumen or a detector current of 2.26×10^{-8} ampere.

The illumination sensor trip point for the star sensor high-voltage inhibit has been set at an output current level of 90 μA. The earth and the sun will cause star sensor high-voltage inhibit. However, the lunar input is insufficient to trip the inhibit circuits. Therefore the star sensor will be on for full lunar illumination. During this interval the star sensor photocathode current is 9.34×10^{-9} ampere. For the lunar image, this will produce a current density of 1.2×10^{-8} ampere/cm^2, which is within the damage-safe limit of 1μA/cm^2.

Page intentionally left blank

5. SATELLITE INTERFACE

The electrical interface between the star sensor and the SAS-B satellite is outlined below.

A Hughes Connector is used as the interface between the satellite harness and the APL star sensor.

The pin allocation of the star sensor side of the Hughes Connector, WS0038P00BN500, is as follows:

Pin No.	Function
1	+10.7V
2	+10.7V Redundant
3	-10.7V
4	-10.7V Redundant
5	+5.0V
6	+5.0V Redundant
7	Power Command Line A
8	Power Command Line B
9	Power Command Line C
10	Ground
11	Ground Redundant
12	Unprocessed Analog Output of Sensor
13	Spare
14	Spare
15	Photomultiplier Power Telltale
16	1 kHz Clock from TLM
17	Aspect No. 1 Readout Gate from TLM
18	Aspect No. 1 Digitized Output of Star Sensor
19	Thermistor Output No. 1
20	Thermistor Output No. 2
21	+10.7V Power On Telltale
22	-10.7V Power On Telltale
23	+5.0V Power On Telltale
24	Ground from SAD
25	Spare

Pin No.	Function
26	Spare
27	Output from SAD
28	Spare
29	Processed Analog Output of APL Star Sensor
30	Aspect No. 2 Read Out Gate from TLM
31	Aspect No. 2 Digital Output of Timing Channel
32	Filter Bandpass Change Command (+10. 7V from Off Side of Command 14)
33	Digitized Output of A/D Converter
34	Spare
35	Filter Bandpass Change Command (+10. 7V from On Side of Command 14)

The pin allocation of the harness side of the Hughes Connector, WSS0038M28BNH02, is as follows:

Pin No.	Function
1	+10. 7V from Battery
2	+10. 7V from Battery
3	-10. 7V from Converter
4	-10. 7V from Converter
5	+5.0V from Converter
6	+5.0V from Converter
7	Power Command Line A (from Command System, Command 36)
8	Power Command Line B (from Command System, Command 36)
9	Power Command Line C (from Command System, Command 36)
10	Ground from Power Ground
11	Ground from Power Ground
12	Unprocessed Analog Output of Sensor to TLM (Experimenter's Analog Housekeeping Channel 11)
13	A/D Reference Voltage to TML (Experimenter's Analog Housekeeping Channel 13) (Not Used)

Pin No.	Function
14	Star Sensor Comparator Reference Voltage to TLM (Experimenter's Analog Housekeeping Channel 14) (Not Used)
15	Photomultiplier Power Telltale to TLM (Experimenter's Analog Housekeeping Channel 45)
16	1 kHz Clock from TLM (Clock C3)
17	Aspect No. 1 Readout Gate from TLM
18	Aspect No. 1 Digitized Output of Star Sensor to TLM (Bits 5-8, Second Syllable of Every Even Minor Frame Word)
19	Thermistor Output No. 1 to TLM (Experimenter's Analog Housekeeping Channel 53)
20	Thermistor Output No. 2 to TLM (Experimenter's Analog Housekeeping Channel 53)
21	+10.7V Power On Telltale to TLM (DSC No. 1, Channel 16, Bit 8)
22	-10.7V Power On Telltale to TLM (DSC No. 1, Channel 16, Bit 7)
23	+5.0V Power On Telltale to TLM (DSC No. 1, Channel 16, Bit 6)
24	Power Return (Ground) from SAD
25	+6.75V to SAD (Not Used)
26	-6.75V to SAD (Not Used)
27	Output from SAD
28	Signal Ground
29	Processed Output of Sensor to A/D Converter
30	Aspect No. 2 Readout Gate from TLM
31	Aspect No. 2 Digitized Output of Timing Channel to TLM (Data Appear on Bits 1-4 of the Second Syllable of Every Minor Frame Word)
32	Filter Bandpass Change Command (+10.7V from Off Side of Command 14)
33	Digitized Output A/D Converter
34	Shield of P58, P15 (Not Used)
35	Filter Bandpass Change Command (+10.7V from On Side of Command 14)
36	Spare
37	Spare
38	Spare

The interface functions outlined above can be classi-
fied in three general categories: command, power, and
telemetry. The individual functions for these categories
are given below.

COMMAND

Pins 7, 8, and 9   Power On Command

These pins connect the power on/off
master relay in the command section to
the two slaved relays in the star sensor
book. The circuitry for this interface
is shown in Fig. 39.

Pins 32 and 35   Filter Parameter Change Command

The command will change the bandpass
filter cutoff frequencies. The command
paralleled with the momentum wheel
on/off command 14. Pin 32 receives
+10.7V from the off side of command
14. Pin 35 receives +10.7V from the
on side of command 14.

POWER SYSTEM INTERFACE

Pins 1, 2, 3, 4,   The power lines input to the star sensor
5, 6, 10 and 11.   (+10.7V, -10.7V, +5.0V) have allowable
variations as listed below:

+10.7V Upper limit 13.0V
     Lower limit 8.8V

-10.7V Upper limit -14.5V
     Lower limit -8.8V
(30 mV ripple, 20 - 40 kHz, load de-
pendent. 100 - 150 mV spikes, 1μs in
width, 20 - 40 kHz repetition rate)

+ 5.0V Upper limit 5.25V
     Lower limit 4.75V
(100 mV ripple, 20 - 40 kHz, load de-
pendent, 100 - 150 mV spikes, 1μs in
width, 20 - 40 kHz repetition rate)
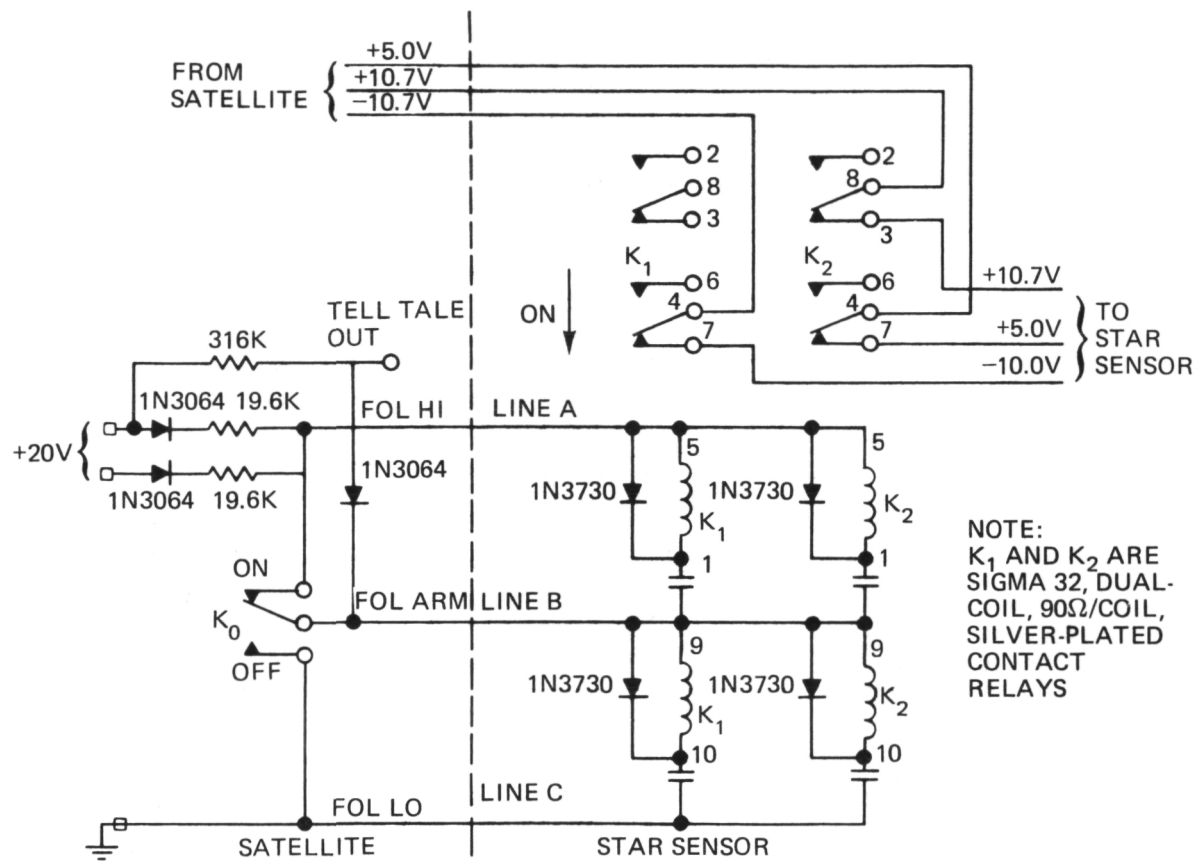
Fig. 39 MASTER-SLAVE RELAY CONTROL

The currents drawn by each of these power lines is:

+10.7V line   21 mA
-10.7V line   11 mA
+ 5.0V line   13 mA

TELEMETRY INTERFACE

Pin 12   <u>Analog Output of Sensor</u>

This monitors the output of the photo-multiplier tube after passing through the first amplifier stage. The output current is transformed into a voltage whose maximum value will be -1.25V. When there is no current output of the photomultiplier tube, the voltage level is +1.25V.

Pin 16   <u>1-kHz Clock Signal</u>

The star sensor uses this signal as the reference for the time measured circuit. The sensor loads this line with a single 54LOO gate.

Pin 18   <u>Digitized Output of Star Sensor to Telemetry</u>

This signal is a four-bit digital word that is proportional to the magnitude of the detected star. It is developed by the A/D converter in the satellite and routed through the star sensor via pins 33 and 18. The four bits are shifted out when ROG-1 goes low. Each bit is sampled when the 1-kHz clock pulse goes high.

Pins 19 and 20   <u>Thermistor Output</u>

The temperature of the photomultiplier tube is monitored and telemetered on the experimenter's housekeeping channel No. 63. The temperature is measured by a Fenwal GB34P92B thermistor connected to the circuit shown in Fig. 40.
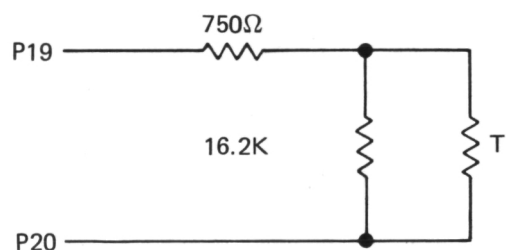
Fig. 40   THERMISTOR MEASURING CIRCUIT

Pins 21, 22, and 23

Power On Telltales

These telltales monitor the switched sensor power lines. When command 36 is on, each line will have the power line voltage (with respect to the ground that it monitors). Each telltale line has a 10K ohm source impedance. When the switch is on, bits 6 to 8 of DSC No. 1 channel 16 will be in a 1 state.

Pin 29

Processed Output of APL Sensor

This is the filtered output of the star sensor. The signal is proportional to the magnitude of the detected star. The signal will vary ±5.0V about 0V. The source impedance of this line is 10K ohms.

Pin 30

Readout Gate No. 2

This signal from the telemetry system reads out the time at which the star transits the reticle slits.

Pin 31

Digital Output of Timing Channel

The time at which the star transits the reticle slit is telemetered on this channel. The information is contained in four digital bits that determine the time to 3 ms. The telemetry samples the signal on the positive going edges of the 1-kHz clock signal when ROG-2 is low.

Pin 33

Digitized Output of the A/D Converter

The output of the satellite A/D converter is routed through the star sensor to telemetry. This pin is to be jumpered to pin 18 in the star sensor.

BIBLIOGRAPHY

J. E. Abate, "Star Tracking and Scanning Systems, Their Performance and Parametric Design," IEEE Trans. on Aerospace and Nav. Elect., September 1963.

C. F. Andren and F. W. Schenkel, A Star Tracker Design for Synchronous Altitude Satellites, APL/JHU TG 869, November 1966.

J. H. Flink, "Star Identification by Optical Radiation Analysis," IEEE Trans. on Aerospace and Nav. Elect., September 1963.

N. P. Laverty, "The Comparative Performance of Electron Tube Photodetectors in Terrestrial and Space Navigation Systems," IEEE Trans. on Aerospace and Nav. Elect., September 1963.

F. V. McCanless, "A Systems Approach to Star Trackers," IEEE Trans. on Aerospace and Nav. Elect., September 1963.

G. Quasius and F. McCanless, Star Trackers and Systems Design, Macmillan Co., 1966.

F. W. Schenkel, "Photometric and Optical Considerations in the DODGE Satellite TV Camera Design," APL Technical Digest, May-June 1967.

Page intentionally left blank

Appendix A

STAR-RETICLE TRAJECTORY COMPUTATIONS AND DERIVATIONS

Assume an "N" shaped slit in conjunction with a photomultipier is used (Fig. 41). The spinning spacecraft causes a star image to cut across the "N". The output signal from the photomultiplier will take the form of a set of pulses having an amplitude corresponding to the magnitude of that particular star passing across the slit. The time interval between pulses from a given star will be measured accurately and used in computing the star position with respect to the spacecraft. The detection threshold of the sensor is adjusted to yield data from a limited number of the brightest stars available. The time intervals of the occurrence of detected stars is also precisely recorded so that star locations with respect to each other as seen from the spacecraft can be determined. Referring to Fig. 41, the equations of motion of a star trajectory crossing the slit may be written as:

$$T_1 = \frac{a_1 \cos(\beta - \alpha_1) + 2b \cos \alpha_1 \cos(\beta - \alpha_1) + c_1 \cos \alpha_1}{2V \cos \alpha_1 \cos(\beta - \alpha_1)}, \quad (A1)$$

$$T_2 = \frac{c_1 \cos \alpha_1 + 2d \cos \alpha_1 \cos(\beta - \alpha_1) + a_1 \cos(\beta - \alpha_1)}{2V \cos \alpha_1 \cos(\beta - \alpha_1)}, \quad (A2)$$

$$T_1 - T_2 = \frac{b-d}{V}, \quad (A3)$$

where:

T_1 is the time interval corresponding to the star trajectory across the slit over a distance, $a/2 + b + c/2$;
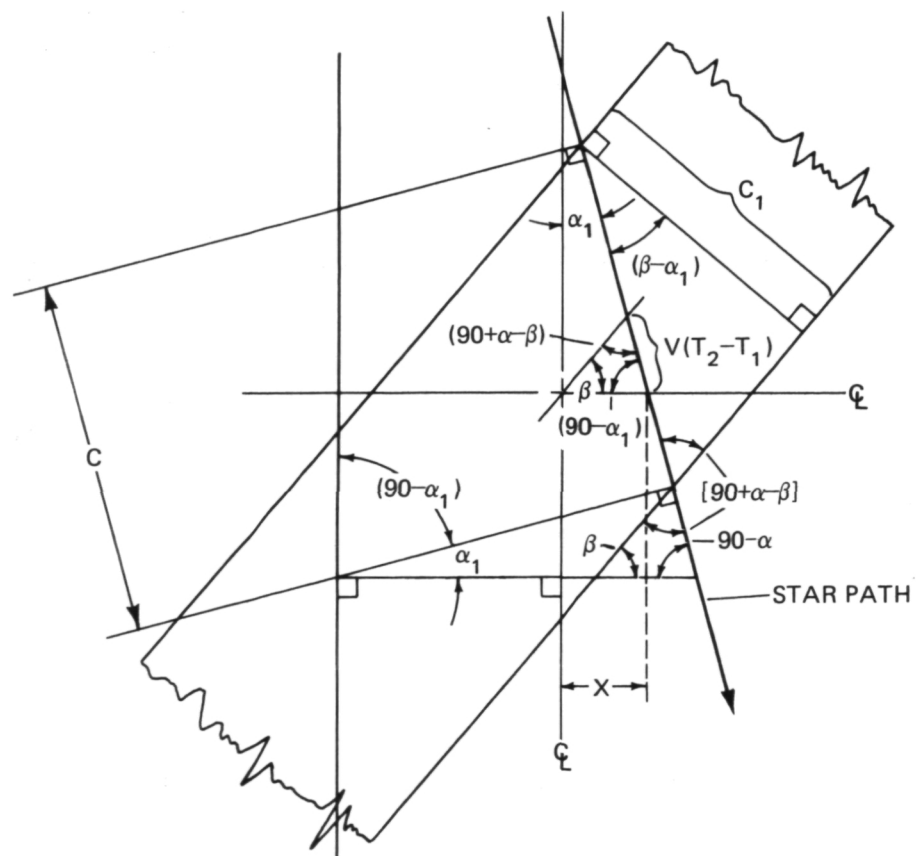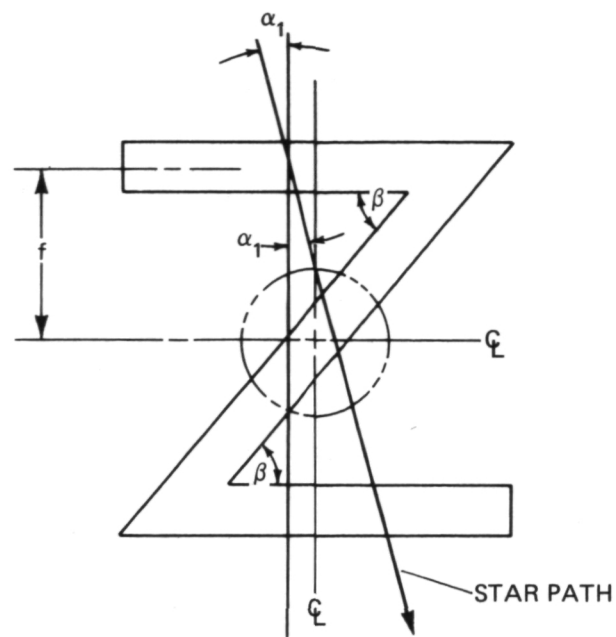
Fig. 41 SLIT GEOMETRY

T_2 is the time interval corresponding to the star trajectory across the slit over a distance, $c/2 + d + e/2$. α_1 is an arbitrary angle that the satellite spin axis could subtend with respect to the "N" mask;

V is the star trajectory velocity as determined by the spacecraft spin velocity.

Also from Fig. 41 the following equation may be written:

$$\cos \alpha_1 = \frac{2f}{(T_1 + T_2)V} \quad . \tag{A4}$$

The sign of α_1 is determined by measuring the time interval, T_3, where:

$$C = VT_3,$$

α_1 is negative if $C < C_1/\cos \beta,$ (A5)

α_1 is positive if $C > C_1/\cos \beta$.

(C_1 is known from the slit geometry.)

To locate a given star with respect to some arbitrary axis in the spacecraft, one can select the center of the "N" slit as a reference. The "N" slit orientation with respect to the spacecraft has been predetermined. Referring to Fig. 41, the value of X may be determined by applying simple trigonometric relationships where X can be positive or negative with respect to the center reference of the "N" slit.

$$X = \frac{V(T_2 - T_1) \cos (\alpha_1 - \beta)}{\sin \beta} \quad . \tag{A6}$$

By knowing X for each star, the time of its occurrence, and the satellite rotational velocity, one can plot a composite star map. A composite map of these star plots for a complete revolution of the satellite spin yield the satellite attitude.

If in Eq. (A3) $T_1 = T_2$ and therefore $b = d$, the star trajectory passes directly through the geometric center of the "N" slit (Fig. 42). For this case, α_1 could have any value. The magnitude of α_1 is determined by the length of T_1 and T_2:

$$T_2 = T_1 = \frac{\alpha_1 \cos(\beta - \alpha_1) + 2b \cos \alpha_1 \cos(\beta - \alpha_1) + c_1 \cos \alpha_1}{2V \cos \alpha_1 \cos(\beta - \alpha_1)}.$$

$$b = \frac{2VT_1 \cos \alpha_1 \cos(\beta - \alpha_1) - a_1 \cos(\beta - \alpha_1) - c_1 \cos \alpha_1}{2 \cos \alpha_1 \cos(\beta - \alpha_1)}. \quad \text{(A 7)}$$

Also:

$$b = \frac{g \sin \beta}{\cos \alpha_1}, \quad \text{(A 8)}$$

and

$$2g \sin \beta = 2VT_1 \cos \alpha_1 - a_1 - \frac{c_1 \cos \alpha_1}{\cos(\beta - \alpha_1)}. \quad \text{(A9)}$$

The last two terms on the right side of the equation are very small and can be neglected to yield:

$$\cos \alpha_1 = \frac{g \sin \beta}{VT_1}. \quad \text{(A 10)}$$

The sign ($\pm$) of α_1 can be determined by the following criterion if α lies between $0°$ and $\pm(90 - \beta)°$. When $C < C_1 / \cos \beta$, α_1 is negative, and when $C > C_1 / \cos \beta$, α_1 is positive, where $C = C_1 / \cos(\beta - \alpha_1)$.

$$b = \frac{g \, \mathrm{SIN}\, \beta}{\mathrm{COS}\, \alpha_1}$$
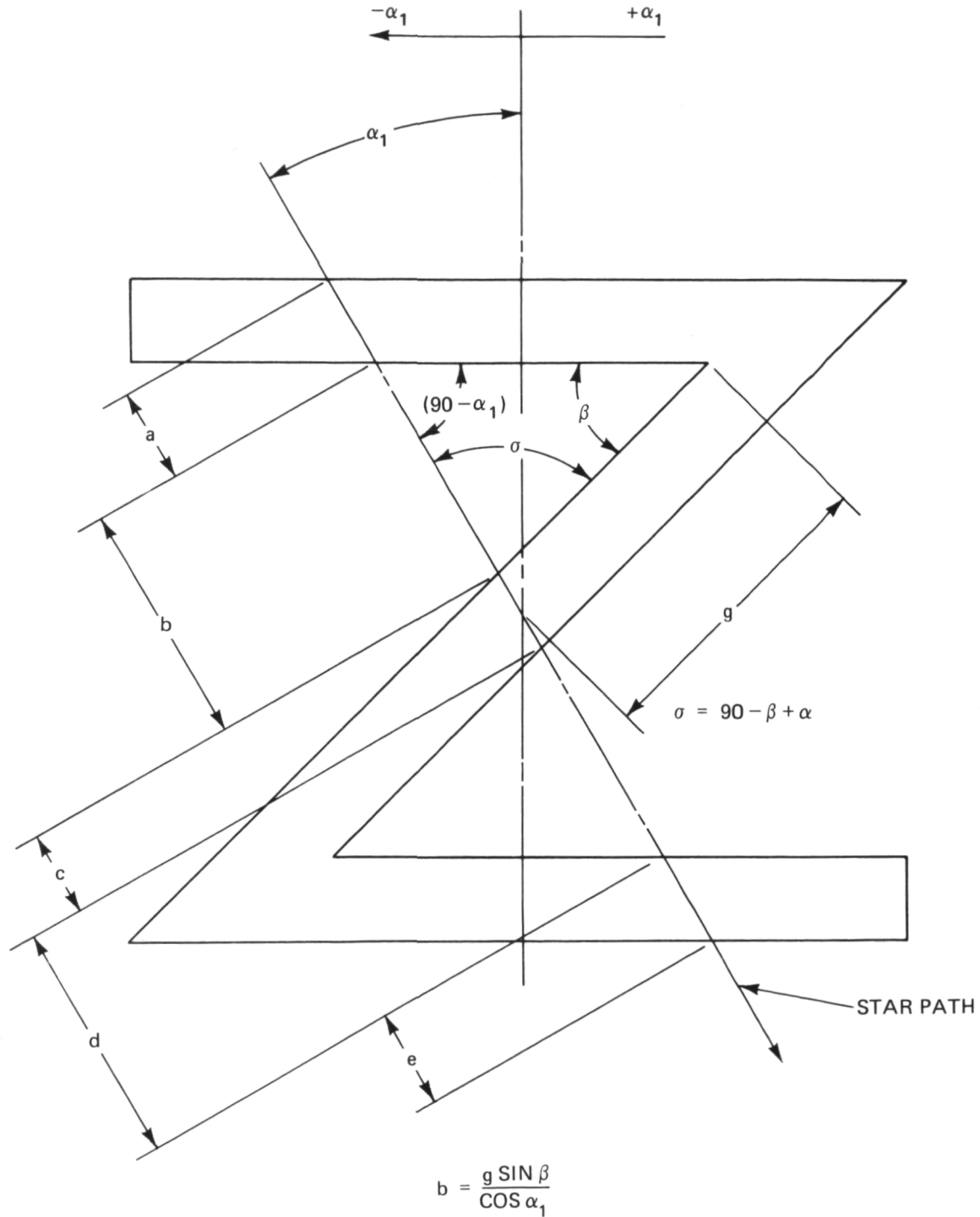
Fig. 42 SLIT GEOMETRY

In most cases, α_1 is zero or very small, and all of the foregoing equations are simplified. If α_1 is known accurately from a ground calibration, the timing of the three pulses uniquely determines the star position independent of the spin velocity, V. The use of Eqs. (A4) and (A6) will yield the required information for plotting the star field, independent of α_1.

Appendix B

DETECTION AND FALSE ALARM

The theoretical signal-to-noise ratio values of 6.2 (in the presence of signal) and 8.1 (in the absence of signal) will be used to examine detection probabilities and false alarm rates in the fast mode.

The postfilter amplitude versus probability curves are shown in Fig. 43.

In the amplitude channel, the major concern is the variability of the output signal in the presence of a fourth magnitude star. We assume that, to a first approximation, the noise amplitude is constant during the pulse width. With an expected fourth magnitude level of 47 mV, σ_2 = 7.6 mV. The $\pm 3\sigma$ variability corresponds to an output signal ranging between 24 and 70 mV. In the slow mode, noise is reduced by $\sqrt{12}$ so that the output signal range is 40 to 54 mV.

In the timing channel, two items connected with threshold detection are desired: a high detection probability coupled with a reasonably low false alarm rate.

The threshold is set at about 1σ below the +4 visual magnitude K0 star level.

From a probability integral table, the detection probability for a +4 (K0 type) star is 84%. (Detection probability is represented by the area under the curve lying to the right of T). This probability rapidly approaches 100% for slight increases in output signal caused by either brighter or bluer stars. For example, a 30% increase in signal strength is produced by a +4 A0 star or a +3.7 K0 star. In this case, the detection probability increases to 99.64%.

$s/\sigma_1 = 8.1$

$s/\sigma_2 = 6.2$
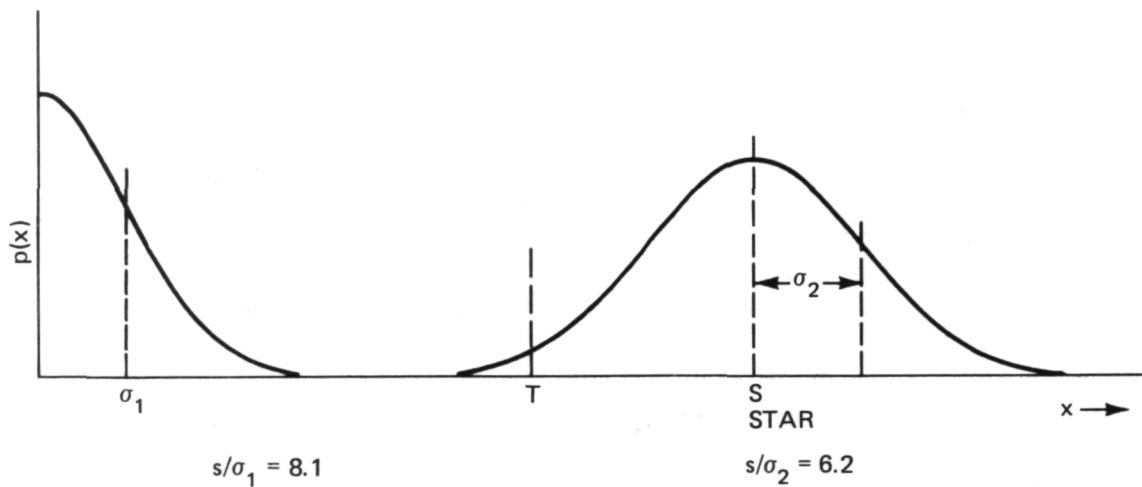
Fig. 43 POSTFILTER AMPLITUDE VERSUS PROBABILITY

False alarm probability is represented by the area under the left hand curve lying to the right of T. To find this value, T must be expressed in terms of σ_1:

$$T = S - \sigma_2 = 8.1\sigma_1 - \frac{8.1}{6.2}\sigma_1 = 6.8\sigma_1 .$$

These values are too large to be read directly from most tables. Instead, an approximation valid for large values of T/σ may be used (see Appendix C):

$$P_{fa} = \frac{e^{-x^2}}{2x\sqrt{\pi}} , \qquad (B1)$$

where:

$$x = \frac{T}{\sqrt{2}\sigma} .$$

This leads to:

$$P_{fa} = \frac{0.98 \times 10^{-10}}{2 \times 4.80 \sqrt{\pi}} = 5.8 \times 10^{-12} .$$

This extremely low false alarm probability will, of course, not be realized because of the presence of circuit noise on the order of a few millivolts.

It is of interest to calculate detection and false alarm probabilities with the Milky Way as background, a condition that also approximates a sun signal equivalent to a second magnitude star. Background current will increase from the average 8.00×10^{-15} ampere to about 50×10^{-15} ampere. Signal-to-noise ratios will deteriorate to:

$$s/\sigma_1 = 3.7 \quad \text{or} \quad \sigma_1 = 12.7 \text{ mV}.$$

$$s/\sigma_2 = 3.45 \quad \text{or} \quad \sigma_2 = 13.6 \text{ mV}.$$

The threshold level is fixed at 39 mV. Detection probability is then 67.2%. To calculate false alarm probabilities:

$$\frac{T}{\sigma_1} = \frac{39}{12.7} = 3.07.$$

This value may be used to enter a probability table, and yields the following result:

$$P_{fa} = 0.00108.$$

Because of the filtering, noise may be considered independent over the interval $1/\beta$, or 9.2 ms. Hence the average time needed to realize one false alarm is:

$$\frac{9.2 \times 10^{-3}}{1.08 \times 10^{-3}} = 8.5 \text{ seconds}.$$

It is planned to use the amplitude channel as the primary star detection channel. When a detection is recorded, the timing channel is then investigated to obtain a precise reading as to time of occurrence. In this case, a false alarm is of no concern except as it interferes with a real star. This will occur whenever a false trigger precedes a star pulse within the same 48-ms sampling period. There are roughly five independent noise samples within the 48-ms period. Half the false triggers will occur after the star pulse and are of no consequence. Hence the interference probability for the sensor is:

$$P_{fa} = 0.00108 \times \frac{5}{2} = 0.0027.$$

MULTIPLE STARS

The foregoing false alarm and interference proba-
bilities are due solely to noise. There is, in addition, the
further possibility of an error in the timing channel caused
by two or more star pulses occurring within the same
48-ms sampling period. For a 5° by 10° field of view, the
three legs of the "N" slit combine to give a total slit length
of 30° perpendicular to the direction of travel. At the high
spin rate of 1 rpm, or 6° per second, the area swept out
during a 48-ms period is 6 by 30 by 0.048 = 8.65 deg^2.
There is, on the average, 0.02 star per deg^2 bright enough
to exceed the sensor's threshold. The average number of
stars exceeding the threshold during a 48-ms period is
therefore 0.17. The probability of multiple occurrences
is given by the Poisson distribution:

$$p(x) = \frac{m^x e^{-m}}{x!}, \tag{B2}$$

where

$\quad$ p(x) = probability of there being exactly x number
$\qquad\quad$ of stars,

$\quad$ m $\,$ = average number of stars = 0.17,

$\quad$ p(0) = 0.844 (probability of finding no stars),

$\quad$ p(1) = 0.143 (probability of finding exactly one
$\qquad\quad$ star).

The probability of a multiple occurrence then is 1 - (0.844 +
0.141) = 0.013, so that of all the star detections, the
probability of a multiple occurrence is 0.013/1 - 0.844 ≈ 8%.
Approximately half of these cases represents a weaker star

following a brighter star where no error ensues.   Thus in
4% of the star detections, an erroneous time is obtained.
Once the star sensor's orientation is known, the trouble-
some star detections can be identified and anticipated.
Furthermore, since the 48-ms sampling period is not
synchronous with the spacecraft spin rate, many of these
errors will not repeat on subsequent scans.

Appendix C

SIGNAL INTEGRATION VERSUS PEAK DETECTION

The required memory feature in the amplitude channel may be obtained by either integration or peak detection. The two methods are here compared. The timing channel operates on signals picked off prior to the memory circuit and so is of no concern in this comparison.

In the presence of a star, the peak detector's superiority is obvious, since the output's variability is not increased by noise integration throughout the sampling period.

Less obvious is the comparison for the condition of noise only. It is meaningless to compare the rms noise output of these two processes since the peak detection is nonlinear, resulting in a non-Gaussion distribution. The proper basis for comparison is the likelihood of exceeding a given level at the sampling instant. The computation is considerably simplified if this level is much greater than 1σ of the incoming noise. This is, in fact, the practical case where the level of interest would be that of a fourth magnitude star and many times greater than the rms noise.

The probability integral as listed in Peirce's Table of Integrals is:

$$\frac{2}{\sqrt{\pi}} \int_0^x e^{-x^2} dx.$$

Since e^{-x^2} is an even function, this integral may be written as:

$$\frac{1}{\sqrt{\pi}} \int_{-x}^{+x} e^{-x^2} dx.$$

The usual form of the normal probability function is:

$$\frac{1}{\sqrt{2\pi}\,\sigma}\; e^{-x^2/2\sigma^2}.$$

Hence the table in Peirce may be thought of as valid for a σ of $1/\sqrt{2}$. To use the table for a threshold level, T, and an rms noise of σ, the value $T/\sqrt{2}\sigma$ must be used as the x entry. The table then gives the probability of the noise lying between +T and -T. Subtracting from unity gives the probability of lying below -T or above +T. Finally, dividing by 2 gives the probability of exceeding +T.

For $T \gg \sigma$,

$$P_{fa} \approx \frac{e^{-x^2}}{2x\sqrt{\pi}}, \qquad \text{(Peirce, p. 120)}$$

where:

P_{fa} = false alarm probability

= probability of exceeding T,

$$x = \frac{T}{\sqrt{2}\sigma}.$$

This is the probability of exceeding T for one independent trial. The noise may be considered to be approximately constant during a period $1/B$ (where B = bandwidth). For the peak detector, the noise gets n independent tries at exceeding T, where $n = \dfrac{\text{sampling period}}{1/B}$. Since P_{fa} is very small, the effect of the peak detector is to increase the false alarm probability by a factor of n.

An integrator effective over this same sampling period will show an increase of σ by a factor $\sqrt{n}$. Hence

in this case, there is only one independent attempt to exceed T but with an increased noise. The probability of exceeding T is now:

$$P'_{fa} \approx \frac{e^{-\frac{x^2}{n}}}{\frac{2x\sqrt{\pi}}{\sqrt{n}}} \qquad \text{(integrator)}$$

whereas for the peak detector:

$$P_{fa} \approx \frac{n\,e^{-x^2}}{2x\sqrt{\pi}} \qquad \text{(peak detector)}.$$

The ratio of these two probabilities is:

$$\frac{P'}{P} \approx \frac{\sqrt{n}}{n}\frac{e^{-\frac{x^2}{n}}}{e^{-x^2}} \approx \frac{e^{x^2(1-\frac{1}{n})}}{\sqrt{n}} \approx \frac{e^{x^2}}{\sqrt{n}}.$$

Hence the peak detector is clearly superior to the integrator.

Page intentionally left blank

Appendix D

STAR SENSOR/EARTH SHINE — MINIMUM
ANGLE OF APPROACH

The trip point for the illumination sensor is set at
90 μA at an illumination angle of 53°. When viewing the
sun, more than adequate protection is afforded the star
sensor. The sun presents a point-like image at the illumi-
nation detector focal plane. On the other hand, the earth
subtends an angle of 134° as viewed from the 500-km satel-
lite altitude. As was shown in Section 4, the earth will
result in a signal of 763 μA output from the illumination
sensor. This is approximately eight times the trip current
for the star sensor inhibit. In other words, the earth
shine must cover approximately one-eighth of the active
detector area of the illumination sensor to cause star sen-
sor inhibit. This means that the earth shine will come to
within approximately 36° of the illumination sensor's refer-
ence axis. This is the approximate minimum angle of
earth shine approach, $\alpha_{min.}$, for star sensor inhibit.
Likewise, the star sensor will be illuminated to within 36°
of its optical reference axis. The star sensor light shade
transfer characteristic indicates an attenuation of about 10^4
for this angle. The current density at the photocathode of
the photomultiplier may then be calculated:

$$ J_{pc} = \frac{B}{4(f/\#)^2} \frac{\beta A_s \tau \text{ (pc sensitivity)}}{A_{pc}} . \tag{D1}$$

If:

B = earth brightness for 50% albedo = 5 $\times$ 10^5 fL,

f/# = speed of objective optic = f/2,

β = optic efficiency = 0.65,

A_s = area of "N" slit = 5.57 $\times$ 10^{-4} ft^2,

τ = light shade transmission at $\alpha_{min.}$ = $\sim 10^{-4}$,

pc sensitivity = 180 μA/lumen,

A_{pc} = photocathode illuminated area = 0.7 cm^2,

J_{pc} = photocathode current density in A/cm^2,

then:

$$J_{pc} = 2.91 \times 10^{-8} \text{ A/cm}^2.$$

This current density value is two orders of magnitude below the maximum permitted to avoid photocathode damage.

Appendix E

MOONSHINE ON EARTH'S SURFACE – REFLECTED FROM EARTH BACK TO SATELLITE

The moonshine on the earth's surface = 4.4×10^{-8} W/cm^2 or 3×10^{-2} fc.

$$E = \frac{E_s RT}{4f^2 (m+1)^2} , \qquad (E1)$$

where:

E = tube face illumination in footcandles,

E_s = scene illumination in footcandles,

R = reflectance of scene,

T = lens transmission,

m = linear magnification from scene to tube face,

f = lens speed (f/#).

The term "m" is negligible when the object-to-lens distance is large compared with the lens focal length.

Let R = 0.5, T = 0.65, f = f/2, and $E_s = 3 \times 10^{-2}$ fc. Then

$$E = \frac{3 \times 10^{-2} (0.5)(0.65)}{(4)(1)} = 24.36 \times 10^{-4} \text{ fc.}$$

The area of "N" slit = 4.48×10^{-5} ft^2.
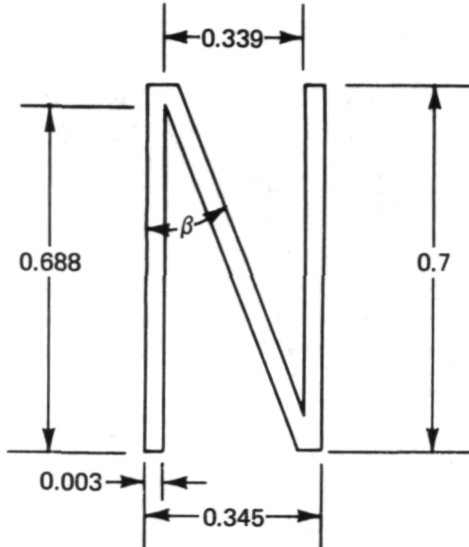
Lumens = A x footcandles

$$= (4.48) \, 10^{-5} \, (24.36) \, 10^{-4} \, fc$$

$$= 1.09 \times 10^{-7} \text{ lumen on photocathode.}$$

pc sensitivity $= 2 \times 10^{-4}$ A/lumen.

pc current = pc sensitivity x lumens

$$= 1.09 \times 10^{-7} \times 2 \times 10^{-4} = 2.18 \times 10^{-11} \text{ ampere.}$$

The pc current density for a 1-cm^2 spot on the photocathode is 2.18×10^{-11} A/cm^2. This level of current density will not result in damage to the photomultiplier photocathode. The detectable signal level from the illumination sensor is on the order of 10^{-9} ampere and is insufficient to cause inhibition of the PMT high-voltage power supply.